

LIGHTHOUSE REPORTS

Propeller-Hull Interaction Effects in waves (part 1)



A research project carried out within the Swedish Transport Administration's industry program Sustainable Shipping, operated by Lighthouse, published in August 2022

Propeller-Hull Interaction Effects in Waves (Part 1)

Authors

Arash Eslamdoost¹, Mohsen Irannezhad¹, Martin Kjellberg²,
Rickard E. Bensow¹

¹Department of Mechanics and Maritime Sciences, Chalmers University of Technology, Gothenburg, Sweden.

²Sweden AB, Gothenburg, Sweden.



CHALMERS



Detta projekt har genomförts inom Trafikverkets branschprogram Hållbar sjöfart, som drivs av Lighthous

Abstract

This study focuses on understanding the propeller-hull interaction effects not only in calm water but also in presence of waves, ranging from short wavelengths up to large wavelengths (wavelengths of 20% up to 300% of the ship length). The propeller performance and the interaction effects between propeller, hull, and ship appendages are different in presence of waves. Due to the complexity of the problem, propeller-hull interaction effects in waves have not been fully understood and thus multiple assumptions are being made during a ship design process based on the knowledge that naval architects have gained from more simplified working conditions, e.g. from calm water model measurements. The study is carried out using computational tools of different fidelity (potential flow solver and viscous flow solver). The results in this report contain a summary of ship motion and added resistance of two different vessels using the aforementioned computational approaches. In this work, as an essential step towards the prediction of interaction effects in waves, bare hull performance prediction in calm water and regular head waves is carried out using two distinct numerical methods. First, a Fully Nonlinear Potential Flow (FNPF) method is used to investigate a ship performance in a broad range of operational conditions. The analysis of the results provided a valuable insight into the ship's hydrodynamic responses and the correlation between them. Subsequently, a state-of-the-art Computational Fluid Dynamics (CFD) method is employed using a Reynolds-Averaged Navier-Stokes (RANS) approach. Besides ship hydrodynamic responses, the results from this method provided detailed information about the flow field around the hull, including its transient nominal wake. In addition, a formal verification and validation (V&V) procedure is applied to understand and control the numerical and modelling errors in the RANS computations. Generally, the results of the employed numerical methods are in good agreement with the experimental data. The prediction of ship motions and to some extent resistance in the FNPF method is rather accurate, however, due to the higher level of simplifications and approximations in this method, the RANS method is deemed a better candidate for the prediction of ship wake. The computational costs of RANS methods are 2-3 orders of magnitude higher than that of FNPF. The ship hydrodynamic responses and the flow field analyses from this work can shed more light on the hull wave interaction effects and help the ship/propeller designers to optimize their designs for more realistic conditions than only calm water.

The continuation of the project, with focus on propeller performance as well as propeller-hull interaction effects in waves, is funded by the administration in the business program Sustainable Shipping through LIGHTHOUSE and started in May 2022.

Sammanfattning

Denna studie fokuserar på att förstå interaktionseffekterna propeller-skrov, inte bara i stilla vatten utan även i närvaro av vågor, allt från korta våglängder upp till stora våglängder (våglängder på 20% upp till 300% av fartygets längd). Propellerns prestanda och interaktionseffekterna mellan propeller, skrov och fartygsbihang är olika i närvaro av vågor. På grund av problemets komplexitet har propeller-skrov interaktionseffekter i vågor inte förstått fullt ut och därför görs flera antaganden under en fartygsdesignprocess baserad på den kunskap som skeppsbyggare har fått från mer förenklade driftsförhållanden, t.ex. stillavattenmodellmätningar. Studien genomförs med hjälp av beräkningsverktyg av olika typ med olika förmågor (potentialflödeslösare och viskösfloeslösare). Resultaten i denna rapport innehåller en sammanfattning av fartygets rörelser och tilläggsotstånd för två olika fartyg med hjälp av de ovan nämnda beräkningsmetoderna. I detta arbete, som ett första steg mot att förutsäga interaktionseffekter i vågor, utförs prediktion av skrovs beteende i lugnt vatten och regelbunden vågor med två distinkta numeriska metoder. Först används en FNPF-metod (Fully Nonlinear Potential Flow) för att undersöka det första fartygs beteende under ett brett spektrum av driftsförhållanden. Analysen av resultaten gav en värdefull insikt i fartygets hydrodynamiska beteende (t.e.x. rörelser och tilläggsotstånd) och sambandet mellan dem. Därefter används en mer avancerad CFD-metod (Computational Fluid Dynamics-metod) baserad på Reynolds-Averaged Navier-Stokes (RANS). Förutom fartygets hydrodynamiska reaktioner gav resultaten från denna metod detaljerad information om strömningen runt skrovet, inklusive dess övergående nominella kölvatten. Dessutom tillämpas en formell verifiering och validering (VV) procedur för att förstå och kontrollera de numeriska felen och modelleringsfelen i RANS-beräkningarna. Generellt stämmer resultaten av de använda numeriska metoderna väl överens med experimentdata. Förutsägelsen av fartygsrörelser och i viss mån motstånd i FNPF-metoden är ganska exakt, men på grund av den högre nivån av förenklingar och approximationer i denna metod anses RANS-metoden vara en bättre kandidat för att förutsäga fartygsvaken. Beräkningskostnaderna för RANS-metoder är 2-3 storleksordningar högre än för FNPF. En bättre förståelse av fartygets rörelser och motstånd i vågor samt förutsägelse av det tidsvarierande flödet in i propellern från detta arbete kan kasta mer ljus över skrovvågsinteraktionseffekterna och hjälpa fartygs/propellerdesignerna att optimera sina konstruktioner för mer realistiska förhållanden än bara stilla vatten.

Fortsättningen av projektet, med fokus på propellerprestanda samt propeller-skrov interaktionseffekter i vågor, finansieras av Trafikverkets branschprogrammet "Hållbar Sjöfart", som drivs av LIGHTHOUSE, och startade i maj 2022.

Acknowledgements

This research is funded by the administration in the business program Sustainable Shipping through LIGHTHOUSE (Swedish Maritime Competence Center). The simulations were performed on resources at Chalmers Centre for Computational Science and Engineering (C3SE) as well as National Supercomputer Center at Linköping University (NSC) provided by the Swedish National Infrastructure for Computing (SNIC). The Maritime Research Institute Netherlands (MARIN) is acknowledged for providing the experimental data.

List of publications

Mohsen Irannezhad, Arash Eslamdoost, Martin Kjellberg and Rickad Bensow (2022). Investigation of ship responses in regular head waves through a Fully Nonlinear Potential Flow approach. Ocean Engineering. Vol. 246.

Mohsen Irannezhad, Martin Kjellberg, Rickad Bensow and Arash Eslamdoost (2021). Towards uncertainty analysis of CFD simulation of ship responses in regular head waves. The 23rd Numerical Towing Tank Symposium, Mülheim an der Ruhr, Germany.

Mohsen Irannezhad, Arash Eslamdoost and Rickad Bensow (2019) Numerical Investigation of a General Cargo Vessel Wake in Waves. The 22nd Numerical Towing Tank Symposium, Tomar, Portugal.

Nomenclature

$1 + k$ Form factor ($-$)

\bar{R}_F Mean frictional resistance in regular waves (N)

\bar{R}_W Mean wave making resistance in regular waves (N)

\bar{S} Mean wetted surface area in regular waves (m^2)

\bar{T} Mean measured thrust in free-sailing self-propulsion model tests in regular waves (N)

\bar{V} Mean measured speed in free-sailing self-propulsion model tests in regular waves (m/s)

Δt Time step size (s)

Δ Mass displacement (kg)

λ Wave length (m)

λ_0 Fundamental wave length (m)

μ Heading angle (deg)

∇ Volume displacement (m^3)

ν Kinematic viscosity of water (m^2/s)

ω Circular wave frequency (rad/s)

ω_E Circular wave frequency of encounter (rad/s)

ϕ Velocity potential (m^2/s)

ρ Water density (kg/m^3)

θ Calm water trim (deg)

θ_i The i^{th} harmonic amplitude of pitch motion response in regular waves (deg)

$\theta_{\varepsilon i}$ The i^{th} harmonic phase of pitch motion response in regular waves (rad) or (deg)

$\vec{\omega}_h$	Angular velocity vector of the hull
\vec{n}	Unit normal vector of the hull surface pointing into the fluid domain
\vec{p}_p	Position vector of a particle on free surface
\vec{r}_h	Radius vector from the hull center of rotation
\vec{u}_h	Linear velocity vector of the hull
A	Wave amplitude $H/2$ (m)
A_i	The i^{th} harmonic amplitude of measured wave height in self-propulsion model tests in regular waves (m)
$A_{\varepsilon i}$	The i^{th} harmonic phase of measured wave height in self-propulsion model tests in regular waves (rad) or (deg)
B	Breadth at mid-ship (m)
C_B	Block coefficient ($-$)
C_F	Frictional resistance coefficient in the ITTC-57 model-ship correlation line ($-$)
C_{AW}	Added wave resistance coefficient ($-$)
F_{Tow}	Longitudinal towing force in model tests (N)
Fr	Froude number ($-$)
g	Gravitational acceleration (m/s^2)
H	Wave height (m)
k	Wave number (rad/m)
K_{yy}	Mass radius of gyration around Y -axis (m)
L	Length between perpendiculars (m)
L_{CG}	Longitudinal position of center of gravity from aft perpendicular (m)
p	Unsteady hydrodynamic pressure (N/m^2)

p_a	Atmospheric pressure (Pa)
r	Response in regular waves
R_F	Frictional resistance in calm water (N)
r_i	The i^{th} harmonic amplitude of ship response in regular waves
R_T	Total resistance in calm water (N)
R_V	Viscous resistance in calm water (N)
R_W	Wave making resistance in calm water (N)
$r_{\epsilon i}$	The i^{th} harmonic phase of ship response in regular waves (rad) or (deg)
R_{Wi}	The i^{th} harmonic amplitude of wave making resistance in regular waves (N)
Re	Reynolds number ($-$)
S	Bare hull wetted surface area at rest (m^2)
S_h	Instantaneous hull wetted surface area in the FNPF computations (m^2)
S_i	The i^{th} harmonic amplitude of wetted surface area in regular waves (m^2)
S_{wet}	Wetted surface area at rest in the respective model test; bare hull plus rudder or all appendages (m^2)
T	Measured thrust in free-sailing self-propulsion model tests in calm water (N)
t	Time (s)
T_A	Draft at aft perpendicular (m)
t_d	Thrust deduction factor ($-$)
T_E	Wave encounter period (s)
T_F	Draft at fore perpendicular (m)
T_z	Heave natural period (s)
T_θ	Pitch natural period (s)

- V Forward velocity (m/s)
- V_{CG} Vertical position of center of gravity from keel (m)
- x_d Computational domain length from fore perpendicular (m)
- x_i The i^{th} harmonic amplitude of surge motion response in regular waves (m)
- y_d Computational domain half breadth (m)
- z Calm water sinkage (m)
- z_i The i^{th} harmonic amplitude of heave motion response in regular waves (m)
- Z_p Vertical position of a point with respect to the undisturbed free surface (m)
- $z_{\epsilon i}$ The i^{th} harmonic phase of heave motion response in regular waves (rad) or (deg)

Contents

1 Objectives	1
2 Structure of the report	2
3 Potential Flow Simulation of Ship Hydrodynamics in Waves	3
3.1 Vessel Geometry and Operational Conditions	7
3.2 Methods	8
3.2.1 Experimental Method	8
3.2.2 Fully Nonlinear Potential Flow Panel Method	11
3.2.3 Design Tool for Estimating Added Wave Resistance	16
3.2.4 Post-processing Techniques	16
3.3 Calm Water Results	18
3.3.1 Sinkage, Trim and Resistance	18
3.3.2 Decay Motions	19
3.4 Regular Wave Results	21
3.4.1 Motion Responses	22
3.4.2 Resistance Responses	31
3.5 Conclusions	40
4 Viscous Flow Simulation of Ship Hydrodynamics in Waves	45
4.1 Vessel geometry and conditions	45
4.2 Numerical modeling	47
4.3 Resistance and motions validation	49
4.4 Propeller wake investigations	50
4.5 Conclusion	53

5	Towards Uncertainty Analysis of CFD Simulation of Ship Responses in Regular Head Waves	54
5.1	Method description	54
5.2	Results and discussion	57
6	Concluding remarks and future work	61
	References	62

1 Objectives

The main objective of this project is to step towards predicting ship powering with a higher accuracy and use our energy resources more efficiently and intelligently. Taking the advantage of the state of the art computational techniques, we want to develop a numerical method which is capable of capturing the sophisticated flow around a self-propelled hull in waves. Then, the method will be used for understanding the physics of propeller-hull interaction effects in waves in a detailed level. Understanding the physics in turn provides us a possibility to map the interaction effects in a systematic way which is missing today. Understanding the propeller-hull interaction effects in waves will provide ship designers with a series of extra information for situations when ships are operating in their actual working conditions rather than only in calm water.

2 Structure of the report

In this report first we discuss a fully-nonlinear potential flow approach for simulation of ship motions and added resistance in waves (Chapter 3). Then application of a viscous method is investigated for simulations of ship hydrodynamics, including motions, added resistance as well as ship wake (Chapter 4) followed by uncertainty analysis of the results from viscous flow simulations (Chapter 5).

3 Potential Flow Simulation of Ship Hydrodynamics in Waves

Ship performance in seaway has been widely investigated experimentally and numerically. However, it is practically impossible to take all of the entailed physics into consideration. Hence, a series of assumptions and simplifications are often introduced in such methods. Traditionally, ship performance in calm water has been the main research topic in ship hydrodynamics. However, calm water is rather an exception in an actual voyage. A seaway may contain waves with various heights and lengths propagating in different directions. Operating in waves may have several effects on ship behavior. The interactions between waves, hull and the propulsion system of a ship may significantly affect the ship motions, resistance, wake and propeller load in comparison to calm water operational conditions. Added resistance due to waves for a ship operating in real sea conditions affects its required engine power in comparison to calm water conditions, which may lead to a noticeable ship performance degradation. Furthermore, large amplitude ship motions in a rough sea may adversely affect the ship structural integrity and harm the crew and cargo. Therefore, ship performance prediction in waves is crucial, especially in the early stages of the ship design process.

Different experimental and numerical methods can be utilized for prediction of ship performance in waves. For instance, the performance can be predicted experimentally through Captive or Free-Sailing (Free-Running) tests in towing tanks or seakeeping basins, ITTC (2018). Although these model tests are expensive and time-consuming, the ship's added resistance and motions are expected to be predicted with a high level of accuracy from the measured motions and towing force (or propeller thrust). On the other hand, since 1950s, computational seakeeping methods have started to evolve. Each method has different level of fidelity with respect to its computational costs and accuracy. Generally, the approach in these methods is based on either Potential Flow methods (Strip Theory or Three-Dimensional Panel Methods) or Computational Fluid Dynamics (CFD) techniques. Bertram (2012) has presented a structured overview of the most well-known ship performance prediction methods.

Usually, potential flow solvers are computationally much faster than CFD solvers. In potential flow methods, the flow is assumed to be inviscid, incompressible and irrotational. In reality, viscosity is significant in seakeeping, especially if the boundary layer separates periodically from the hull, e.g., in the case of roll and yaw motions, Bertram (2012). However, in the cases where the viscous effects are insignificant, application of potential flow methods may provide a great advantage in terms of computational efficiency. One of such scenarios is studying a ship performance in head waves in which the main ship motion responses are surge,

heave and pitch which are found to be less affected by viscosity. Moreover, in potential flow solvers based on panel methods, only the boundaries are required to be discretized, not the whole fluid domain. This considerably reduces the effort needed for grid generation; however, the simple and continuous free surface defined in potential flow solvers is not capable of modeling wave breaking, splashes or viscous phenomena. Generally, empirical values for some viscous effects can play a complementary role in these methods. Contrary to potential flow methods, the state-of-the-art CFD methods have the advantage of predicting ship hydrodynamic responses more accurately by performing high fidelity nonlinear computations with fewer simplifications related to the flow physics. However, these methods are computationally expensive and time-consuming. Therefore, based on the specific problem under study and the level of complexities required, one should choose a suitable numerical method for the ship performance prediction. Since the investigations performed in this part of the work are meant to study a ship bare hull hydrodynamic responses in regular head waves, the utilization of a potential flow method is found to be beneficial enabling investigation of a broader range of operating conditions. The results of such studies can be used for understanding the overall behavior of the ship in regular head waves and eventually help out to choose more critical operational conditions to be studied in more details using higher fidelity CFD solvers.

In potential flow methods, the Laplace equation is solved in conjunction with considerations of appropriate ship hull and free surface boundary conditions. Potential flow methods are often classified based on the levels of nonlinearities applied to these boundary conditions. These methods, based on ITTC (2017) categorization, include linear potential flow methods, Froude-Krylov nonlinear methods (weakly nonlinear methods), body exact methods (or weak scatterer methods) and fully nonlinear methods. In linear potential flow methods, the linearized boundary conditions are represented in terms of the mean free surface and wetted surface area. Then the solution of Boundary Value Problem (BVP) is the superposition of different potential components (steady, incident wave, radiation and diffraction). Linear potential flow methods are often fast, efficient, robust and easy to use in a practical sense. Another advantage of using linear potential flow methods is the possibility of solving the problem in frequency domain, which offers a very low computational cost in comparison to the unsteady methods. In weakly nonlinear and body exact methods, nonlinearities are introduced to a certain extent in order to increase the solution accuracy. When the free surface boundary conditions are applied without any simplifications or approximations, it is commonly referred as Fully Nonlinear Potential Flow (FNPF) method.

The FNPF methods represent the category of potential flow methods with the least amount of approximations to the potential flow and the interactions between the ship hull and the fluid. The term "Fully Nonlinear" in such

methods should not be confused with the Fully Nonlinear viscous flow methods indicated in the taxonomy of hydrodynamic solutions explained by Hirdaris et al. (2016), as the FNPF methods are counted as potential flow methods and hence, the nonlinear phenomena associated with the fluid in the form of viscosity are neglected. In these methods, the aspects of violent flow incidences, such as slamming, is not considered. The FNPF methods fall into the category of "Smooth Waves" in the aforementioned taxonomy which fill the gap between the partially nonlinear potential flow and fully nonlinear viscous flow methods. Moreover, it is assumed that the waves are "smooth" in the FNPF methods, therefore, wave breaking or fragmentation of the fluid domain (e.g., green water on deck) can not be modelled in such methods. Furthermore, in the current FNPF method, the hull is assumed to be rigid, hence the hull flexibility and hydroelasticity as a result of fluid-structure interaction are not investigated.

Although there are several FNPF methods developed in recent years, these methods are not extensively used to investigate the hydrodynamic responses of ships in waves. For instance, water waves are simulated by a fully nonlinear potential flow method developed by Engsig-Karup et al. (2009) which is further developed by Ducrozet et al. (2010) to study the wave-wave and wave-structure interactions for a fixed circular cylinder. A fully nonlinear potential flow method is developed by Mola et al. (2017) to evaluate the performances of different hulls in calm water. Coslovich et al. (2021) studied the KVLCC2 tanker motions and resistance responses in waves using an FNPF method focusing mainly on adaptive grid refinement and nonlinear decomposition of the velocity potential and wave field. In order to provide a comprehensive understanding of the physics of ship hydrodynamics in waves, in the current study, we have employed a fully nonlinear unsteady three-dimensional potential flow solver, SHIPFLOW MOTIONS. The ship responses, including the motions and wave making resistance and their harmonics, have been investigated in a broad range of operational conditions which leads to an evaluation of capabilities of the employed FNPF method in this context.

Added resistance is the time-average of the longitudinal force (in the opposite direction of movement) on a ship in waves minus the force in calm water at the same forward speed. It demonstrates higher order nature than motions, hence more difficult to be determined, Bertram (2016). The added resistance value is relatively small in comparison to the amplitude of the instantaneous wave exciting force, Faltinsen (1990), thus a high degree of accuracy is required for prediction of added resistance in both experiments and numerical computations, Sadat-Hosseini et al. (2013). Moreover, the dependency of added resistance on ship motions, ship speed, wave length, wave height, wave heading angle, hull form and bow shape makes its accurate prediction even more challenging, Wu (2013). Two major contributors to added resistance in waves are radiation from generated

waves due to ship motions and diffraction and reflection of the incident wave. Fully nonlinear interaction between incident and radiated/diffracted waves is considered in the current FNPF method.

Two main analytical formulations for prediction of added resistance in potential flow methods are known as far-field method and near-field method, ITTC (2018). The far-field methods are based on conservation of energy and momentum. The first far-field method was introduced by Maruo (1957) and Maruo (1960). The method was further developed by Joosen (1966) as well as Newman (1967). Other far-field methods have also been developed by Gerritsma and Beukelman (1972) in which the added resistance was estimated based on the radiated energy method. The near-field methods are based on integration of hydrodynamic pressure on the hull surface. This method was first introduced by Havelock (1937) and further developed in Havelock (1942) based on the Froude-Krylov approach for calculation of wave induced pressure forces acting on the hull. Other examples of well-known near-field methods are presented in Boese (1970), Salvesen (1978) and Faltinsen et al. (1980). Most of the aforementioned methods are based on Strip Theory. Ship motions are playing a significant role in the formulation of these analytical methods. Therefore, ship motions are supposed to be estimated prior to the prediction of added resistance. In the Strip Theory, ship motions are generally obtained in frequency domain based on the Slender Body Theory. On the other hand, modern potential flow methods (e.g., Three-Dimensional Panel Methods) are often divided into time-domain or frequency-domain and Green Functions or Rankine panel methods, ITTC (2017). SHIPFLOW MOTIONS is a time-accurate three-dimensional potential flow solver using Rankine source distribution where both the free surface and hull are discretized. In this FNPF solver, the added resistance is computed based on a near-field method from the direct pressure integration on the hull wetted surface area. The rigid body motions equations are also solved.

The main objective of this part of the work is to study the hydrodynamic performance of a vessel in terms of resistance and motion responses in a range of operational conditions by an FNPF method, and compare the results against experimental data. For comparison, the added wave resistance is also computed with a design tool by Martinsen (2016), through linear interpolations from an added resistance transfer function database. This database has been created by combining radiated energy method and the near-field asymptotic approach for different geometries in a range of Froude numbers and heading angles. The test case under study in this part of the work is a general cargo vessel developed in LeanShips¹, which is designed with a “tunnel-shaped” aft configuration meant to accommodate a Large Diameter Propeller (LDP). The concept of transforming a ship conventional-sized propeller to an LDP was introduced in order to improve the vessel propulsive efficiency;

¹Low Energy And Near to zero emissions Ships (LeanShips), is an EU-funded project, 2015-2019. More information about Large Diameter Propeller demo case can be found in <https://www.leanships-project.eu/demo-cases/demo-case-09/overview>.

however, the LDP vessel peculiarities regarding its design and efficiency characteristics are not taken into consideration as part of the current study objectives.

3.1 Vessel Geometry and Operational Conditions

The LDP vessel main particulars in model-scale and in two loading conditions are given in Table 1. In this study, the hydrodynamic performance of the vessel operating in fresh water with the density of $\rho = 998.3 \text{ kg/m}^3$ and the kinematic viscosity of $\nu = 1.018E - 06 \text{ m}^2/\text{s}$ is investigated at different advancing speeds presented in Table 2.

Table 1: Model-scale LDP vessel main particulars (scale factor = 27).

Symbol	Loading Conditions		Unit	Denotation
	Full	Ballast		
L	7.95		(m)	Length between perpendiculars
B	0.88		(m)	Breadth at mid-ship
T_F	0.296	0.118	(m)	Draft at fore perpendicular
T_A	0.296	0.259	(m)	Draft at aft perpendicular
∇	1.743	1.089	(m ³)	Volume displacement
Δ	1740	1087	(kg)	Mass displacement
S	10.24	8.46	(m ²)	Bare hull wetted surface area at rest
C_B	0.842	0.825	(-)	Block coefficient
L_{CG}	3.94	3.59	(m)	Longitudinal position of COG from aft perpendicular
V_{CG}	0.344	0.258	(m)	Vertical position of COG from Keel
K_{yy}	1.99	1.95	(m)	Mass radius of gyration around Y-axis (pitch)

Table 2: Vessel speeds in model-scale and the respective Froude numbers $Fr = V/\sqrt{gL}$.

Froude	Fr (-)	V (m/s)
Fr_0	0.00	0.01
Fr_1	0.09	0.79
Fr_2	0.10	0.89
Fr_3	0.11	0.99
Fr_4	0.13	1.19
Fr_5	0.16	1.39
Fr_6	0.18	1.58

An earth-fixed coordinate system as well as a ship-fixed coordinate system are used. The earth-fixed Cartesian coordinate system is considered to be located at the initial mean free surface with X -axis pointing from the ship's bow towards its stern and Z -axis pointing upwards. The ship-fixed Cartesian coordinate system is located at the vessel Center of Gravity (COG) with X -axis pointing astern and Z -axis pointing upwards. Consequently, positive surge motion occurs when the COG moves in the opposite direction of the ship's forward speed. Positive heave motion is defined as when the COG moves upwards and positive pitch motion is defined as

when the ship's bow moves upwards (or stern moves downwards).

The investigations are mainly concerned with the vessel in deep water subjected to regular head waves, however, the vessel performance in calm water is also presented. An overview of the operational conditions in regular head waves is presented in Table 3 in which wave heights H and wave lengths λ are non-dimensionalized by the ship length L . Each of these operating conditions are labelled with a code which are used later as plot legends in Section 3.4. Prior to the model tests, it was predicted that propeller ventilation/emergence may occur frequently for the LDP due to its proximity to the free surface. Since one of the goals of the experiments was the ventilation risk assessment, ballast condition (with a lower draft at the aft perpendicular and hence higher risk of ventilation) was studied more in detail in the measurements.

Table 3: Operational conditions in regular head waves. Non-dimensional wave lengths λ/L in **bold** text are representing equivalent conditions in both self-propulsion model tests (SP EFD) and Fully Nonlinear Potential Flow computations (FNPF).

Loading Conditions	Fr (-)	H/L (-)	Condition Label	λ/L (-)	
				SP EFD	FNPF
Full	0.10	0.014	$Fr_2 - H_2$	0.28	0.28 , 0.55, 0.70, 0.79, 0.91, 1.06, 1.24
		0.028	$Fr_2 - H_4$	0.70, 0.79, 0.91, 1.06, 1.24	0.28, 0.40, 0.51, 0.55, 0.61, 0.70, 0.79, 0.91, 1.06, 1.24 , 1.35, 1.53, 2.04
	0.18	0.014	$Fr_6 - H_2$	-	0.20, 0.28, 0.55, 0.70, 0.79, 0.91, 0.97, 1.06, 1.17, 1.24, 1.35, 1.53, 3.06
		0.028	$Fr_6 - H_4$	-	0.20, 0.28, 0.55, 0.70, 0.79, 0.83, 0.91, 0.97, 1.02, 1.06, 1.17, 1.24, 1.35, 1.53, 2.04, 3.06
Ballast	0.10	0.014	$Fr_2 - H_2$	0.91, 1.06, 1.24	0.37, 0.55, 0.70, 0.79, 0.91, 1.06, 1.24 , 1.35, 1.53
		0.007	$Fr_4 - H_1$	0.79, 1.06, 1.24	0.55, 0.70, 0.79 , 0.91, 1.06, 1.24 , 1.35, 1.53
	0.13	0.014	$Fr_4 - H_2$	0.28, 0.37, 0.49, 0.55, 0.70, 0.79, 0.91, 1.06, 1.24	0.28, 0.37, 0.49, 0.55, 0.70, 0.79, 0.91, 1.06, 1.24 , 1.35, 1.53
		0.021	$Fr_4 - H_3$	0.79, 1.06, 1.24	0.49, 0.70, 0.79, 1.06, 1.24 , 1.35, 1.53

3.2 Methods

3.2.1 Experimental Method

Experimental model tests in calm water and in regular head waves were performed by Maritime Research Institute Netherlands (MARIN). The wooden model is manufactured at MARIN. The calm water model tests

were carried out at Fr_1 , Fr_3 , Fr_4 , Fr_5 and Fr_6 in two different setups (rudder-equipped bare hull and self-propelled model) and the results for Fr_2 were interpolated. During the calm water tests, the model was free to heave and pitch. For the first setup, the resistance test was carried out based on towing the rudder-equipped bare hull by a towing carriage, in which the measured towing force is the vessel total resistance R_T . Based on the decomposition of resistance in ITTC-78 method mentioned by Larsson and Raven (2010), the total resistance is divided into a viscous resistance component $R_V = (1 + k)R_F$, which includes the form effect on friction and pressure, and a wave making resistance component R_W as,

$$R_T = (1 + k)R_F + R_W. \quad (1)$$

The frictional resistance R_F can be computed from,

$$R_F = 0.5\rho S_{wet}V^2C_F, \quad (2)$$

in which the wetted surface area at rest S_{wet} includes the wetted surface area of the configured rudder plus that of bare hull. The frictional resistance coefficient C_F can be computed from the ITTC-57 model-ship correlation line,

$$C_F = \frac{0.075}{(\log Re - 2)^2}, \quad (3)$$

where $Re = VL/\nu$ is the Reynolds number. The calm water wave making resistance R_W then can be deduced from Equation 1 considering the experimentally and numerically (double-body viscous flow) obtained form factor of $1 + k = 1.167$. The resistance test results of the rudder-equipped bare hull are labelled as TOW EFD henceforth.

The calm water model tests were also carried out for the self-propelled model, in which the model was equipped with a propeller while it was unloaded by means of a tow force to compensate for the difference in viscous resistance between model-scale and full-scale. The calm water propeller thrust T , the towing force F_{tow} as well as the dynamic sinkage z and trim θ were measured from these tests. The calm water thrust deduction factor t_d at each respective loading condition and forward speed is then obtained from,

$$t_d = 1 - \frac{R_T - F_{Tow}}{T}, \quad (4)$$

where R_T is the measured total calm water resistance for the rudder-equipped bare hull. On the other hand, the model tests in regular head waves were carried out at the given Froude numbers in Table 3 solely in six Degrees of Freedom (6DOF) in free-sailing self-propelled and self-steered mode. The model acceleration/deceleration in the beginning/end of each run were performed using a towing system consisting four lines controlled under tension or slack by four remotely-operated winches. The model's six degrees of freedom and speed were measured by means of optical tracking systems at a sampling rate of 100 Hz . Thrust and torque were measured by strain gauge transducers at 4800 Hz sampling frequency. Moreover, wave elevation was measured by a resistance type wave probe at a sampling frequency of 200 Hz . The measured harmonic amplitudes and phases of the ship forward speed, ship motions, incident wave height and the propeller thrust were provided. The mean wave making resistance component in regular waves \bar{R}_W is then deduced from the mean thrust in regular waves \bar{T} as,

$$\bar{R}_W = (1 - t_d)\bar{T} - (1 + k)\bar{R}_F, \quad (5)$$

in which t_d and \bar{R}_F need special considerations.

It is well-established that the propulsion factors such as wake fraction and thrust deduction for a ship operating in waves deviate from those of calm water, for instance by Gerritsma et al. (1961), Moor and Murdey (1970) as well as Nakamura and Naito (1975). The deviation is more significant when the ship motions are severe. In the case of LDP vessel, the deviation might be even more pronounced because of the proximity of the propeller to free surface and hence high occurrence of propeller ventilation/emergence in severe conditions, associated with a sudden change in propeller thrust and torque. Due to the lack of knowledge about how exactly the propulsion factors change for the LDP vessel in waves, the thrust deduction factor in Equation 5 is assumed to be equal to the calm water t_d value at the same loading condition and forward speed. A similar assumption is considered by Taskar et al. (2016b) and Valanto and Hong (2017) for studying the propulsion performance of KVLCC2 tanker and a cruise ship in waves, respectively. Block (1993) also mentioned that the thrust deduction factor obtained in calm water can be applied to the ships in moderate sea-states. Furthermore, since the model was running in free-sailing self-propulsion mode, the mean value of the measured speed \bar{V} was not exactly equal to the expected V in Table 2. Therefore, a linear interpolation is used for estimation of the thrust deduction

factor at the mean attained speed \bar{V} in regular waves from the previously computed calm water t_d in Equation 4. Moreover, the Reynolds number in Equation 3 and accordingly C_F in Equation 2 are calculated for the mean attained speed \bar{V} in each respective model test. \bar{R}_F in waves is then calculated assuming the same wetted surface area and hence similar frictional resistance in waves as in calm water at each certain loading condition and forward speed. S_{wet} includes the wetted surface area of the bare hull and all other appendages presented in the self-propulsion model tests. The self-propulsion model tests results are labelled as SP EFD henceforth.

3.2.2 Fully Nonlinear Potential Flow Panel Method

A fully nonlinear unsteady three-dimensional potential flow solver SHIPFLOW MOTIONS (Version 6) is used for the numerical computations. The flow in potential flow methods is assumed to be homogeneous, inviscid, incompressible and irrotational. A scalar quantity referred as velocity potential ϕ of which satisfies Laplace's equation $\nabla^2\phi = 0$ is used to describe the flow. In FNPF methods, fully nonlinear kinematic and dynamic boundary conditions are applied on the free surface as,

$$\frac{D\vec{p}_p}{Dt} = \nabla\phi, \quad (6)$$

$$\frac{D\phi}{Dt} = -gZ_p + \frac{1}{2}\nabla\phi \cdot \nabla\phi - \frac{P_a}{\rho}, \quad (7)$$

in Lagrangian frame where D is the material derivative ($\frac{D}{Dt} \equiv \frac{\partial}{\partial t} + \nabla\phi \cdot \nabla$), $\vec{p}_p = (X_p, Y_p, Z_p)$ is the position of a particle on the free surface in the earth-fixed coordinate system, Z_p is the vertical position of the particle with respect to the undisturbed free surface and P_a is the atmospheric pressure. Moreover, an impermeability condition is applied on the rigid hull surface taking into account the hull motions,

$$\frac{\partial\phi}{\partial n} = \vec{n} \cdot (\vec{u}_h + \vec{\omega}_h \times \vec{r}_h), \quad (8)$$

where \vec{n} is the unit normal vector of the hull surface pointing into the fluid domain, \vec{u}_h and $\vec{\omega}_h$ are the linear and angular velocity vectors of the hull and \vec{r}_h is the radius vector from the hull center of rotation. Impermeability condition is also applied on the bottom of the computational domain.

Then, the BVP (defined by the Laplace's equation and the boundary conditions) is solved using a Boundary

Element Method (BEM). The hull surface and computational domain are discretized by means of flat quadrilateral panels assuming constant strength source distribution. Green Functions are used to obtain the source strength. The fully nonlinear free surface boundary conditions introduce a time dependency into the problem. Therefore, the free surface boundary conditions equations are integrated in time to evolve the free surface position and velocity potential using a Mixed Eulerian-Lagrangian (MEL) method in which each time step is divided into two sub-steps. Evolution of the free surface and velocity potential in time is tracked by markers associated at each panel. In the Eulerian sub-step, the boundary value problem is solved using the BEM and the velocity potential and the velocity of the free surface markers are obtained in the domain. In the Lagrangian sub-step, the boundary conditions are integrated in time and the free surface position and velocity potential are updated for the next time step.

In order to avoid unwanted wave reflections from the boundaries of the computational domain an artificial damping zone is introduced away from the hull. In this zone, the perturbed part of the solution is blended with the analytically described undisturbed wave field, hence matching the computed solution to the solution of the known wave field at the boundaries. Moreover, the FNPF method is not able to handle wave breaking and in the case of occurrence, the computations will stop immediately. Wave breaking is a natural phenomenon that occurs when waves become too steep, for instance it may be seen around the bow and stern of ships. In the current FNPF method, the waves that are about to break are identified and suppressed to prevent breaking, hence the smooth wave assumption is considered. The unsteady hydrodynamic pressure is calculated at any point in the domain from the unsteady Bernoulli equation,

$$p = -\rho \left(\frac{\partial \phi}{\partial t} + \frac{1}{2} |\nabla \phi|^2 + gZ_p \right), \quad (9)$$

in which the time derivative term is evaluated using a finite difference second order backward scheme. In this way, the nonlinear interactions between the diffracted and radiated wave components as well as the fully nonlinear incident wave field are implicitly taken into account. The hydrodynamic forces and moments acting on the body are computed by integration of the hydrodynamic pressure over all the surface elements dS of the wetted surface area of the hull S_h as,

$$\vec{F} = - \iint_{S_h} p \vec{n} dS, \quad (10)$$

$$\vec{M} = - \iint_{S_h} p (\vec{r}_h \times \vec{n}) dS. \quad (11)$$

Then the rigid body motions equations are solved representing the equilibrium between the inertial, gravitational and hydrodynamic forces and moments. For more details about this FNPF method and free surface modeling see Kjellberg (2013).

All of the FNPF simulations are carried out for the LDP vessel bare hull in 3 degrees of freedom (3DOF) where the hull is free to surge, heave and pitch, except in the 1DOF heave/pitch decay motions simulations. Calm water simulations are carried out at Fr_1 to Fr_6 to obtain the sinkage and trim as well as the calm water wave making resistance R_W . Moreover, decay motion simulations in calm water are performed at Fr_0 , Fr_2 and Fr_6 in 1DOF as well as in 3DOF. Since the specification of zero ship velocity is not possible in the current FNPF solver, a minor velocity ($V = 0.01 \text{ m/s}$) is used in the simulations at Fr_0 (Table 2). The 5th order Stokes regular head waves with fuller troughs and sharper crests than airy (linear) waves are introduced at the inlet of the computational domain. These Stokes waves were found to be a better resemblance of the real-world waves, Fenton (1985). Other important computational specifications in the FNPF solver are discussed in the following sections.

Computational Domain The size of computational domain is calculated based on the respective Froude number in each simulation. Taking advantage of a symmetry boundary condition, only half of the domain is considered in the simulations. The potential flow computations in SHIPFLOW MOTIONS are scale-independent, therefore, all the computations are carried out for the ship with unit length (i.e. geometry non-dimensionalized by the ship length). An overview of the computational domain is shown in Figure 1. The domain dimensions are defined as the normal distances to the ship fore perpendicular in which x_d/L and y_d/L are the boundaries edges in longitudinal and transverse directions, respectively. The domain is made wide enough to cover the Kelvin wedge over the considered domain length.

Hull Discretization In the FNPF method, the complete hull is discretized and remains body-fixed during the computations to allow for large variation of wetted surface. The hull discretization is done based on the best practices for hull panelization in potential flow methods in order to appropriately capture the form of the hull. The hull panel distribution is shown in Figure 2 where the non-dimensional distance from the fore perpendicular (x/L) is also shown. The number of panels on the half of the hull used in the FNPF simulations is 6747.

Free Surface Discretization In the current version of the FNPF solver the panelization on the free surface cannot be modified locally meaning that any modification of the free surface panel size results in change of

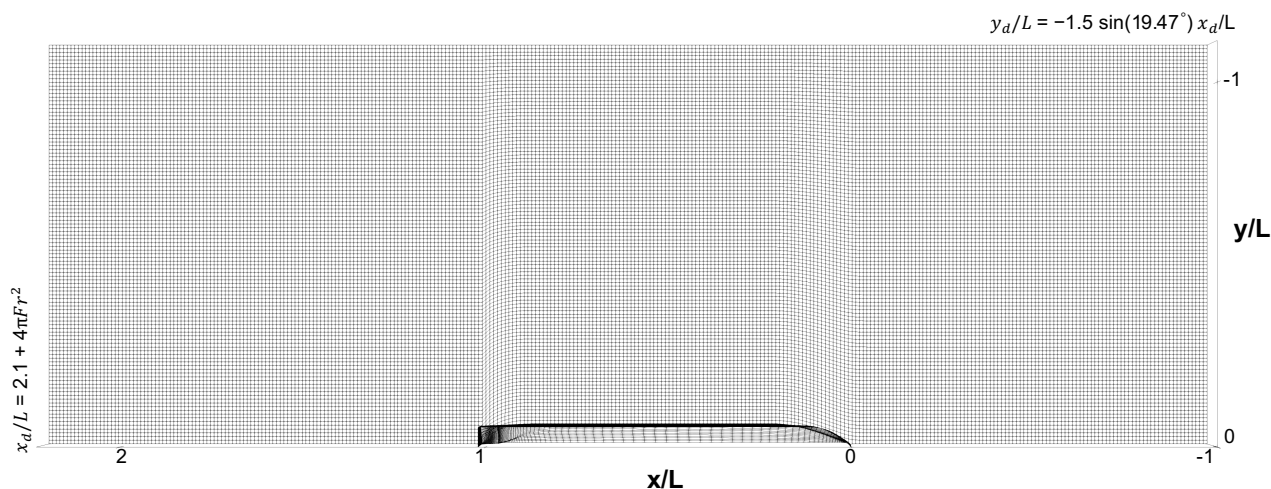


Figure 1: Computational domain overview.

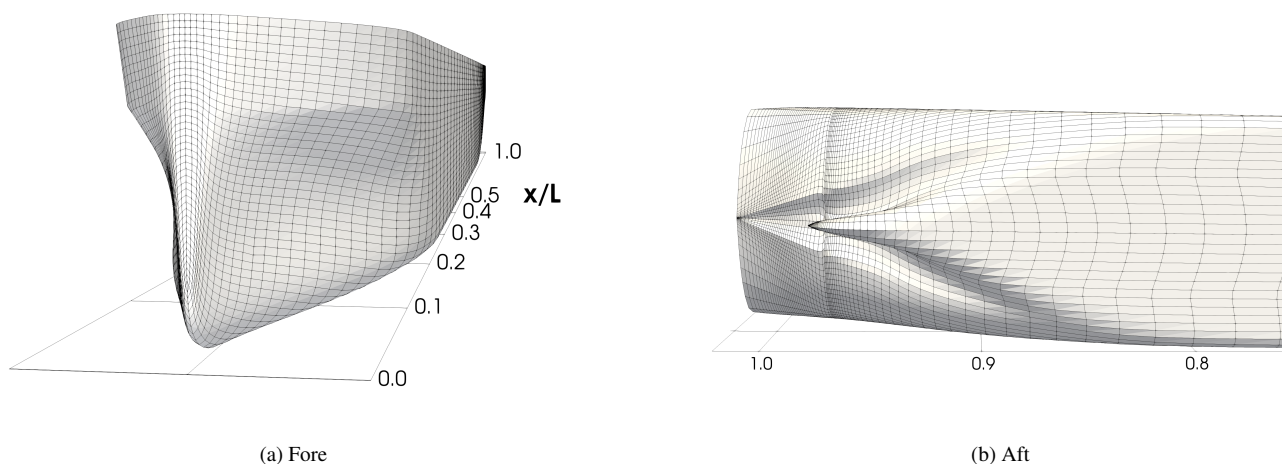


Figure 2: Hull panelization overview.

the size of all panels everywhere in the domain. In order to keep the free surface panelization error as low as possible, a panel size sensitivity analysis has been carried out. These simulations are performed for an operational condition in regular head waves for the fully-loaded ship at Fr_2 . Wave height $H/L = 0.028$ and wave length $\lambda/L = 0.79$ as well as the hull panelization presented in Section 3.2.2 remain the same in all of these simulations while uniformly refining the free surface panels. It is believed that the wave making resistance as well as the motion responses are fairly large for the selected case (Fully-loaded, $Fr_2 - H_4$ and $\lambda/L = 0.79$ in Table 3) which makes this case a suitable candidate for the free surface panelization study.

The results are post-processed based on the techniques explained in Section 3.2.4. The 0^{th} harmonic amplitude of wave making resistance as well as the 1^{st} harmonic amplitudes of heave z_1 and pitch θ_1 motions are shown in

Figure 3. The wave making resistance clearly reaches an approximate convergence by increasing the number of panels on free surface. The convergence of heave and pitch motions are less pronounced since the magnitudes of changes are very small for these motions. These results reveal that free surface panelization has a larger impact on the wave making resistance rather than the motions. The results obtained by the free surface panel distribution at Fr_2 and represented by 32754 panels are considered to be in the asymptotic range and thus the same panelization setup is used for the rest of the simulations in this work. The free surface panels for this case are shown in Figure 1. The panel size in both longitudinal and transverse directions is approximately 1% of the ship length. The total number of panels (including the hull panels) in half domain for Fr_1 to Fr_6 are approximately between 39000 and 47000.

In linear wave theory, the fundamental wave length generated by a ship at constant speed is $\lambda_0 = 2\pi Fr^2 L$ (notice that $L = 1$ in the current FNPF simulations as the ship is scaled based on its length). Due to very small Froude numbers in this study, the criterion of keeping the free surface panels smaller than 5% of the fundamental wave length suggested by Larsson and Raven (2010) would result in extremely small panels, hence very high computational costs. Therefore, this criterion is not fulfilled in this study.

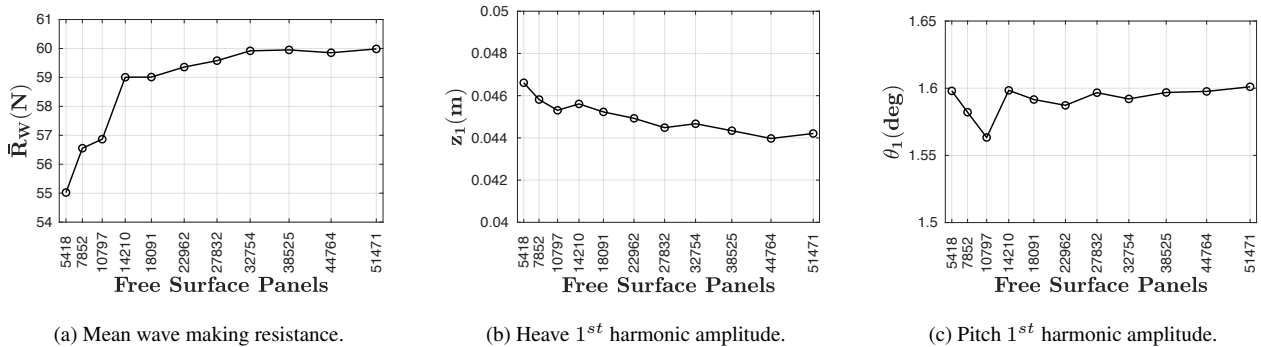


Figure 3: Free surface panelization study of the fully-loaded ship at $Fr_2 - H_4$ and $\lambda/L = 0.79$.

Time Step Size The computational time step size is determined to be a function of fundamental wave period $\sqrt{\lambda_0 2\pi/g}$. In the following simulations, 60 time steps per each wave period is used as the criterion for determining the time step size,

$$\Delta t = \frac{2\pi Fr \sqrt{L/g}}{60}, \quad (12)$$

in which $L = 1$ in the current FNPF simulations. Therefore, time step size becomes only a function of Froude number. In the case of approximately zero speed Fr_0 , the time step size is computed based on $Fr = 0.05$.

Convergence Criteria and Computational Costs The simulations in calm water is deemed converged when the standard deviation of the wave making resistance time history drops below 1% of its rolling tail-weighted root mean square value (last 60% of the signal). The convergence criterion for simulations in waves is defined as when the standard deviation of the mean wave making resistance response signal drops below 1% of its root mean square value in the trailing last two encountered wave periods.

The simulations are carried out using parallel processing on multiple cores on a desktop workstation equipped with an Intel® Core™ i7-8700 CPU @ 3.20 GHz processor base frequency. The computational cost for an individual simulation in this work (using FNPF) is approximately 20 to 80 core-hours depending on the Froude number, incoming wave characteristics and other operational conditions. However, a viscous flow simulation in similar conditions may require two to three orders of magnitude higher computational cost in terms of core-hours based on the data presented by Irannezhad et al. (2019) for the same hull in regular head waves using Unsteady Reynolds-Averaged Navier-Stokes (URANS) simulations as well as by Larsson et al. (2014) and Hino et al. (2021) for different geometries using various viscous flow computations.

3.2.3 Design Tool for Estimating Added Wave Resistance

Added wave resistance of the LDP vessel is also estimated by a design tool developed at Technical University of Denmark (DTU) by Martinsen (2016). In this tool, added wave resistance was calculated for different combinations of geometries at various Froude numbers and heading angles to form a database. The added wave resistance in frequency domain was computed from Salvesen (1978) radiated energy method (5DOF Strip Theory) for long waves and Faltinsen et al. (1980) near-field asymptotic approach for short waves forming a continuous curve at their intersection. Then, five input parameters (L/B , $B/Draft$, C_B , Fr and heading angle μ) are used to carry out a linear interpolation within the validity range of the database to predict the added wave resistance, Martinsen (2016). Since it is not possible to assign different values for the fore and aft draft, the draft in ballast condition is considered as the averaged value, $(T_F + T_A)/2$. The computed added wave resistance from the design tool is labelled as TOOLBOX in the results.

3.2.4 Post-processing Techniques

In order to post-process the time-series of resistance and motions responses $r(t)$ computed in the simulations in waves, Fourier analysis is performed as,

$$r(t) = r_0 + r_1 \cos(\omega_E t + r_{\varepsilon 1}) + r_2 \cos(2\omega_E t + r_{\varepsilon 2}) + r_3 \cos(3\omega_E t + r_{\varepsilon 3}) + \dots, \quad (13)$$

where r_i is the i^{th} harmonic amplitude of the response r , and $r_{\varepsilon i}$ is the phase component related to i^{th} harmonic amplitude. The circular wave frequency of encounter ω_E is computed based on the circular wave frequency ω , ship velocity V and its heading angle μ as,

$$\omega_E = \omega - \frac{\omega^2 V}{g} \cos(\mu), \quad (14)$$

where $\mu = 180^\circ$ for head waves. The wave encounter period T_E is then computed as $T_E = 2\pi/\omega_E$. The Fourier analysis is carried out over the last two encountered wave periods of the response signals when the simulation is converged, see Section 3.2.2. On the other hand, the Fourier analysis on experimental data was performed by MARIN and the harmonic amplitudes and phases of the ship forward speed, ship motions, incident wave height and propeller thrust were provided.

The i^{th} harmonic amplitudes of surge and heave motions are non-dimensionalized by the wave amplitude (x_i/A and z_i/A). Pitch motion harmonic amplitudes are non-dimensionalized based on θ_i/kA in which θ_i is the pitch i^{th} harmonic amplitude in radian and $k = 2\pi/\lambda$ is the wave number. The added wave resistance coefficient C_{AW} is computed from,

$$C_{AW} = \frac{\bar{R}_W - R_W}{\rho g B^2 A^2 / L}, \quad (15)$$

where \bar{R}_W is the mean wave making resistance component in regular waves, R_W is the calm water wave making resistance, B is the ship breadth and A is the wave amplitude. As mentioned in Section 3.2.1, since the model tests in waves were carried out in free-sailing self-propulsion mode, the mean value of the measured speed \bar{V} slightly deviated from the intended speeds in Table 2. Therefore, experimental \bar{R}_W is calculated for the mean measured speed using Equation 5 with the aforementioned special considerations for t_d and \bar{R}_F , see Section 3.2.1. Moreover, calm water wave making resistance R_W at the mean measured speed \bar{V} is obtained through interpolation of the measured calm water R_W at the speeds listed in Table 2.

Moreover, the incident wave height experienced by the ship is different in the measurements and computations. Although the incident wave height in the computations remains relatively close to the specified wave height at

the inlet boundary, in the model tests the wave height experienced by the ship slightly varies from one test to another. The incident wave height in experiments was measured by a wave probe located approximately 2.4 *m* ahead of the fore perpendicular and 3.4 *m* towards the port side of the hull center plane. The Fourier analysis was performed on the measured wave height and the harmonic amplitudes and phases were provided. In order to calculate the experimental non-dimensional harmonic amplitudes of motions and C_{AW} , the experimental wave height $H(t)$ profile is expressed as,

$$H(t) = A_0 + A_1 \cos(\omega_E t + A_{\varepsilon 1}) + A_2 \cos(2\omega_E t + A_{\varepsilon 2}) + A_3 \cos(3\omega_E t + A_{\varepsilon 3}), \quad (16)$$

where A_i and $A_{\varepsilon i}$ are the i^{th} harmonic amplitude and phase of the measured wave height and ω_E is the wave encounter frequency based on the mean attained speed \bar{V} in each respective model test. Then the experimental wave amplitude A is derived from,

$$A = \frac{H^{max} - H^{min}}{2}, \quad (17)$$

in which H^{max} and H^{min} are the maximum and minimum (peak and trough) values of the wave height profile in each respective model test.

3.3 Calm Water Results

3.3.1 Sinkage, Trim and Resistance

The results of calm water wave making resistance, sinkage and trim are shown in Figure 4. A good agreement between the potential flow computed wave making resistance and the experimental data is seen in the fully-loaded condition, except an over-prediction at the highest Froude number and minor under-predictions at the lower Froude numbers. The under-prediction is more pronounced in the ballast condition over the whole range of Froude numbers, which also resulted in rather small negative values of resistance at the lower Froude numbers (these results are not shown in the plot). The wave making resistance is obtained from the integration of considerably large pressure values over the instantaneous wetted surface area of the hull. This increases the risk of error in the lower speed range where the total wave making resistance is small. Alternatively, far-field methods can be employed to overcome this issue. Generally, this kind of numerical errors in conjunction with the discretization errors, as seen in Section 3.2.2, as well as the potential flow simplifications and the use

of empirical formulas, such as ITTC-57 skin friction line, are the main sources of discrepancy between the computed and the measured results. Moreover, the uncertainty related to the experimental data should not be forgotten. In order to be consistent in the computation of added wave resistance, the negative calm water wave making resistance values at the lower Froude numbers are considered to be zero.

The computed sinkage and trim and especially their trends at different Froude numbers are in a good agreement with the experimental data considering the very small values, see Figures 4b and 4c. It should be noted that the experimental data for sinkage and trim are related to the self-propulsion model tests (SP EFD), while only bare hull is considered in the FNPF simulations.

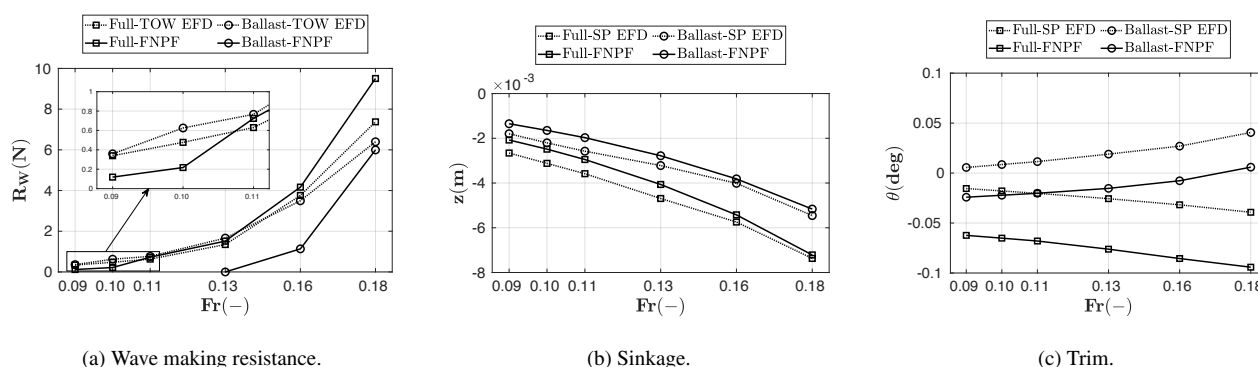


Figure 4: Comparison of the computed resistance, sinkage and trim with the measured values in calm water.

3.3.2 Decay Motions

Lewis (1989) noted that the most significant features of the heave and pitch Response Amplitude Operators (RAOs) to a large extent are dictated by their natural periods. In order to estimate the ship's natural periods of heave T_z and pitch T_θ motions, a series of free heave and pitch decay motion simulations are performed in the fully-loaded condition at Fr_0 , Fr_2 and Fr_6 in 1DOF and 3DOF, see Figure 5. The initial heave is approximately 0.08 m and the initial pitch is 3 deg for all of the cases. Besides, extra heave and pitch decay simulations are carried out at Fr_0 with 3DOF where the initial heave and pitch are set to approximately 0.12 m and 4 deg, respectively. In order to obtain the natural periods, four different intervals between the peaks and troughs of the decay curves, as presented in Figures 5a and 5b, are extracted and shown in Figures 5c and 5d. The gray symbols belong to the cases with higher initial heave and pitch values which give relatively similar results as of the smaller initial values; indicating a negligible effects from initial values on natural periods. The uncertainty of capturing the precise time intervals in which the peaks and troughs of the decay curves occur depends on the time step size. The time step size varies at different Froude numbers, see Section 3.2.2, and

at worst situation may introduce an error up to $2\Delta t$ (one numerical time step error for each captured peak or trough) in the computations of natural period intervals for the unit ship length $L = 1$. In such situations, the maximum error may reach 0.03 s (at the highest Fr) in the calculation of natural period intervals for the results shown in Figure 5.

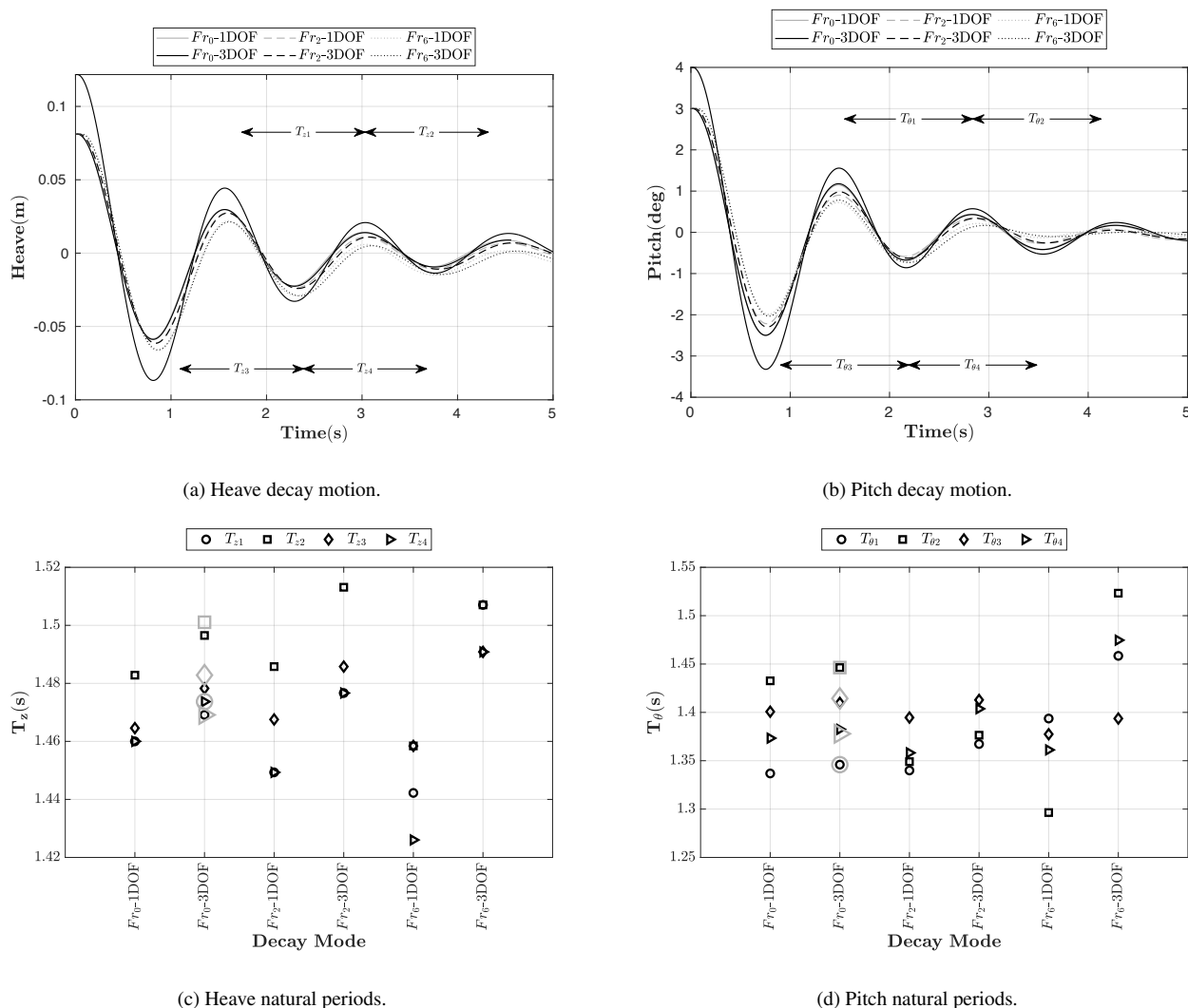


Figure 5: Free decay motions time-series and computed natural periods in fully-loaded conditions. Gray markers in (c) and (d) are for larger initial heave and pitch cases.

It can be seen that the motion coupling slightly increases both heave and pitch natural periods at all Froude numbers. Although there are some minor effects related to forward speed, the trend of such effects is not similar in all of the cases. These differences may originate from the fact that the non-zero forward speed introduces sinkage and trim which can for instance alter the underwater geometry of hull, water plane area and block coefficient and consequently the dynamics of the ship. This can be confirmed considering that the final heave and pitch motions amplitudes converge to zero for the cases with zero speed when the motions are

totally decayed, but these values are non-zero (i.e., equal to sinkage and trim derived in Section 3.3.1) for the cases with non-zero forward speeds. Wu (2013) mentioned that the forward velocity effects on natural periods of motions are negligible. The effects seen in the current study are also small and they might be negligible considering the possible error introduced by the time step size.

It is interesting to study the vessel heave and pitch responses in regular head waves when the wave encounter period is close to heave and pitch natural periods. Since the aim of this study is to investigate the behavior of the vessel in waves, the exact value of heave and pitch natural periods are not of a critical importance per se. In order to be consistent, natural periods of heave and pitch motions are approximated through averaging the calculated values for all Froude numbers in 3DOF (only small initial values), which gives $T_z \approx 1.488$ s and $T_\theta \approx 1.416$ s in the fully-loaded condition. Similarly, free heave and pitch decay simulations in 3DOF at Fr_0 , Fr_2 and Fr_6 are also performed in the ballast condition and the natural periods are approximated as $T_z \approx 1.307$ s and $T_\theta \approx 1.177$ s. The same method is used for averaging, but since the motions decay faster in the ballast condition, only two periods T_{z1} and T_{z3} for heave and $T_{\theta1}$ and $T_{\theta3}$ for pitch are considered. As it can be confirmed in the studies by Lewis (1989) and Wu (2013), the larger block coefficient in the fully-loaded condition gives larger heave and pitch natural periods in comparison to the ballast condition.

3.4 Regular Wave Results

All of the potential flow computations in waves are carried out for the bare hull in 3DOF in the 5th order Stokes regular head waves. Then the hydrodynamic performance of the vessel is analyzed. An overview of the operational conditions in waves is given in Table 3. Resistance and motions as the main ship responses are investigated and the simulation results are compared against the available self-propulsion 6DOF model test data. Ship responses in waves are mainly influenced by the wave forces (and moments) exerted on the hull. Wave excitation forces and radiation forces form the total wave forces acting on the hull in the presence of waves. The forces exerted on the restrained hull in waves which excite the motions are called wave excitation forces. Radiation forces are due to the motions of the ship which is forced to oscillate in calm water. In the current FNPF computations, the total forces (and moments) acting on the ship are calculated from the pressure integration on the wetted surface area of the hull and the force decomposition into different components is not possible.

Fourier analysis is used to evaluate the time-series of the responses. It should be noticed that, the mean velocity \bar{V} and hence the encounter wave frequency in the self-propulsion model tests are slightly different than the

simulation encounter wave frequency, see Section 3.2.1. Moreover, the wave amplitude A used for non-dimensionalization of the harmonic amplitudes of motions and added wave resistance in the FNPF method is the theoretical 5th order stokes wave amplitude, while for SP EFD data A is derived from the wave height measurements explained in Section 3.2.4. The regular head wave results are presented in model-scale.

3.4.1 Motion Responses

The 0th harmonic amplitudes of surge, heave and pitch motions are relatively small and almost equal to the values observed in their respective operational conditions in calm water. The 1st harmonic amplitudes of these motions are the dominating components in the Fourier analysis of the response signals, whereas higher order components are close to zero. Generally, the amplitudes and phases of wave excitation and radiation forces, which form the total wave forces, determine the motion responses of the ship in different conditions. In the following, different motion responses of the ship in regular waves are analyzed in which the 1st and 2nd harmonic amplitudes of motions are considered. It should be pointed that the harmonic amplitudes of motions derived from the model tests are rounded which turned the small values of the 2nd harmonic amplitudes of motions into zero.

Surge Motion The surge motion response of the ship is shown in Figures 6 and 7 for the fully-loaded and ballast conditions, respectively. The magnitude of the 1st harmonic surge motion x_1 is rather small except for very long waves, where the wave excitation surge forces are expected to be large. At the same Froude number, x_1 increases by increasing wave height, see Figures 6a and 7a. Very small local peaks are seen especially in the fully-loaded condition, see Figures 6b and 7b, where the wave encounter frequency is close to the heave and pitch natural frequencies ($\omega_z \approx 4.22 \text{ rad/s}$ and $\omega_\theta \approx 4.44 \text{ rad/s}$ in fully-loaded condition and $\omega_z \approx 4.81 \text{ rad/s}$ and $\omega_\theta \approx 5.34 \text{ rad/s}$ in ballast condition). This might be an indication of strong motion coupling within that range of encounter frequencies. On the other hand, these local peaks occur in the vicinity of $\lambda/L = 0.70$ for most of the studied operational conditions, see Figures 6a and 7a, which may reflect the effects of wave excitation surge forces near such wave lengths. In other words, these local peaks may occur due to the nearly matching lengths of the incident wave and the parallel mid-body (the distance between fore and aft shoulders). More investigations near such wave lengths are motivated for different hull types.

The non-dimensional 1st harmonic amplitude of surge motion, shown in Figures 6c and 7c, indicates an approximate linear relation of the 1st harmonic surge motion response to wave amplitude A , as the cases

with similar Froude number and different wave heights have almost similar x_1/A . The non-dimensional 2nd harmonic amplitude of surge motion, shown in Figures 6d and 7d, are rather small compared to x_1/A . Since the surge motion response of the vessel is rather insignificant, any possible numerical errors can significantly affect the results. Therefore, drawing a more solid conclusion about surge motion response would involve a high level of uncertainty.

The importance of accurate surge prediction for ships operating in waves has been discussed in literature. For instance, Joncquez et al. (2008) stated that the influence of surge motion on added wave resistance of a bulk carrier is insignificant. Moreover, Sadat-Hosseini et al. (2013) found that for KVLCC2 vessel the effects of surge motion on added wave resistance was negligible in their numerical computations, however, their model tests under free and fixed conditions revealed that the pitch motion and added wave resistance are influenced in certain conditions. Yu et al. (2017) also mentioned that the prediction of surge motion is important due to the coupling between surge, heave and pitch motions. Therefore, accurate prediction of surge motion would be beneficial to enhance the prediction accuracy for other ship responses in waves. Generally, for the LDP vessel a good agreement between the FNPF computational results and experimental data is seen for the surge motion response of the ship in Figures 6 and 7.

Heave Motion The heave motion response of the ship in both loading conditions is shown in Figures 8 and 9. The 1st harmonic amplitude of heave motion is relatively larger in the longest waves, see Figures 8a and 9a. There are clearly local maxima near the resonance condition in Figures 8b and 9b, i.e., when the encounter wave frequency is close to $\omega_z \approx 4.22 \text{ rad/s}$ in the fully-loaded condition and $\omega_z \approx 4.81 \text{ rad/s}$ in the ballast condition. The wave encounter frequency of the local peak at Fr_2 (Figure 9b) is under-resolved in the computations meaning that more simulations are required in the vicinity of $\omega_z \approx 4.81 \text{ rad/s}$ to capture the trend of heave resonance. The heave resonance in the ballast condition is more pronounced, resulting in considerably large heave motion responses.

The comparison of the non-dimensional 1st harmonic amplitude of heave motion between the cases with the same Froude number and different wave heights in Figures 8c and 9c, reveals an approximate linear relation between the heave 1st harmonic amplitude z_1 and the wave amplitude. However, this relation does not hold in the near resonance region in the fully-loaded condition, see e.g., Fr_6-H_2 and Fr_6-H_4 in Figure 8c. Irvine et al. (2008) also mentioned that the nonlinear effects for pitch and heave motions of a surface combatant vessel were evident near resonance conditions as z_1/A and θ_1/kA showed wave steepness dependencies in those situations.

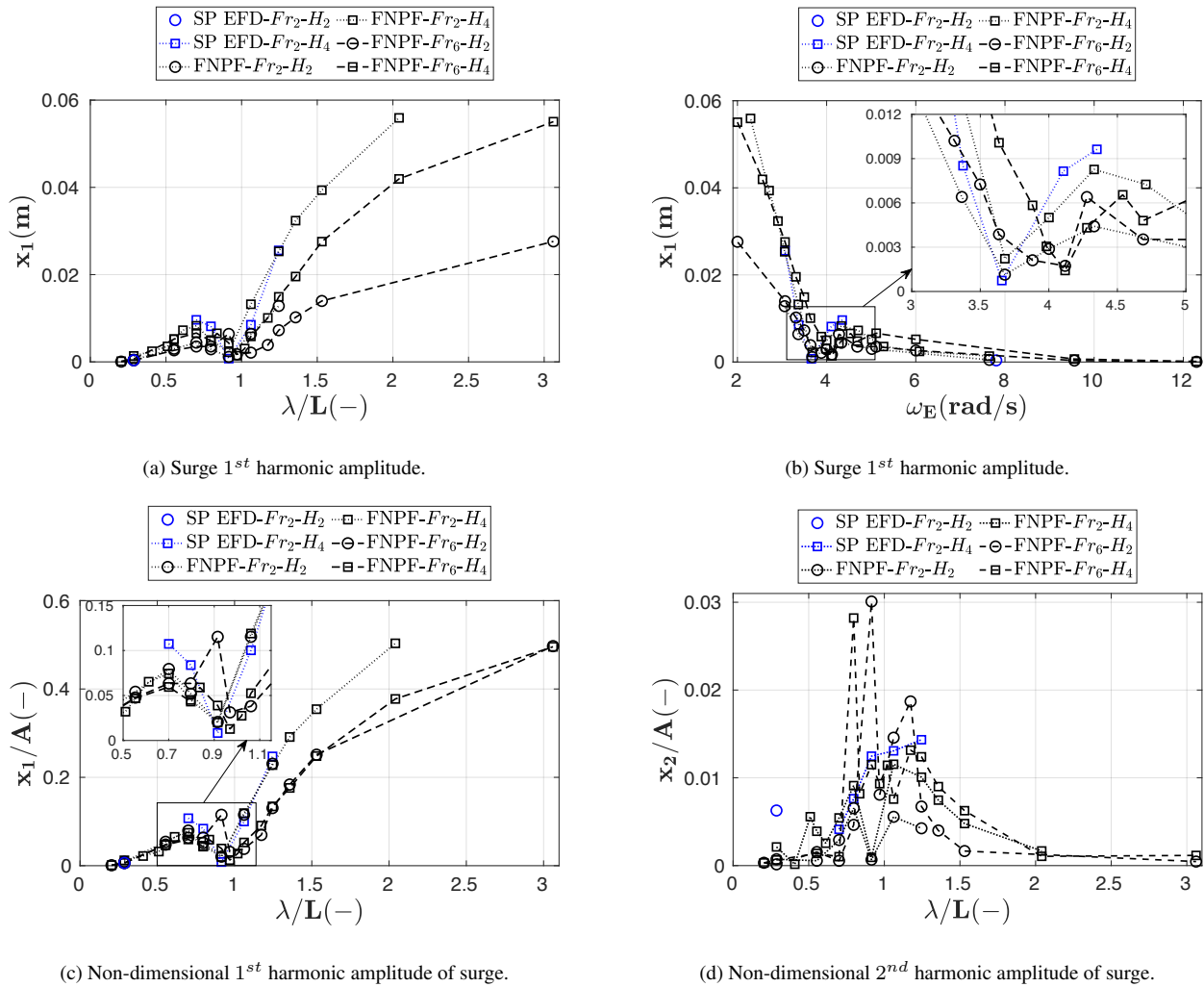


Figure 6: Comparison of the computed surge motion response with the measured values in regular head waves in fully-loaded condition.

Generally, for the LDP vessel, larger z_1/A arise for the cases with the same wave height and higher Froude numbers. The heave excitation force is expected to increase by increasing wave length and the maximum heave excitation force often occurs in extremely long waves. For the LDP vessel, the maximum may occur around $\lambda/L = 3.06$ as the computed z_1/A at Fr_6 exceeds 1 in the fully-loaded condition but the result obtained for $\lambda/L = 3.5$ (not included in the plots) shows reduction of z_1/A to 1 again. Very small z_2/A values are seen in Figures 8d and 9d compared to z_1/A . The non-dimensional 2nd harmonic amplitude of heave motion increases by decreasing ω_E in both loading conditions but it decreases again in very long waves. Since z_2 values from the experimental data are rounded, the small values obtained from the ballast conditions are turned into zero. The potential flow results for the heave motion response agree quite well with the available experimental data. The largest discrepancies of z_1/A are seen at $\omega_E \approx 3.37 \text{ rad/s}$ in the fully-loaded condition and at the resonance in the ballast condition.

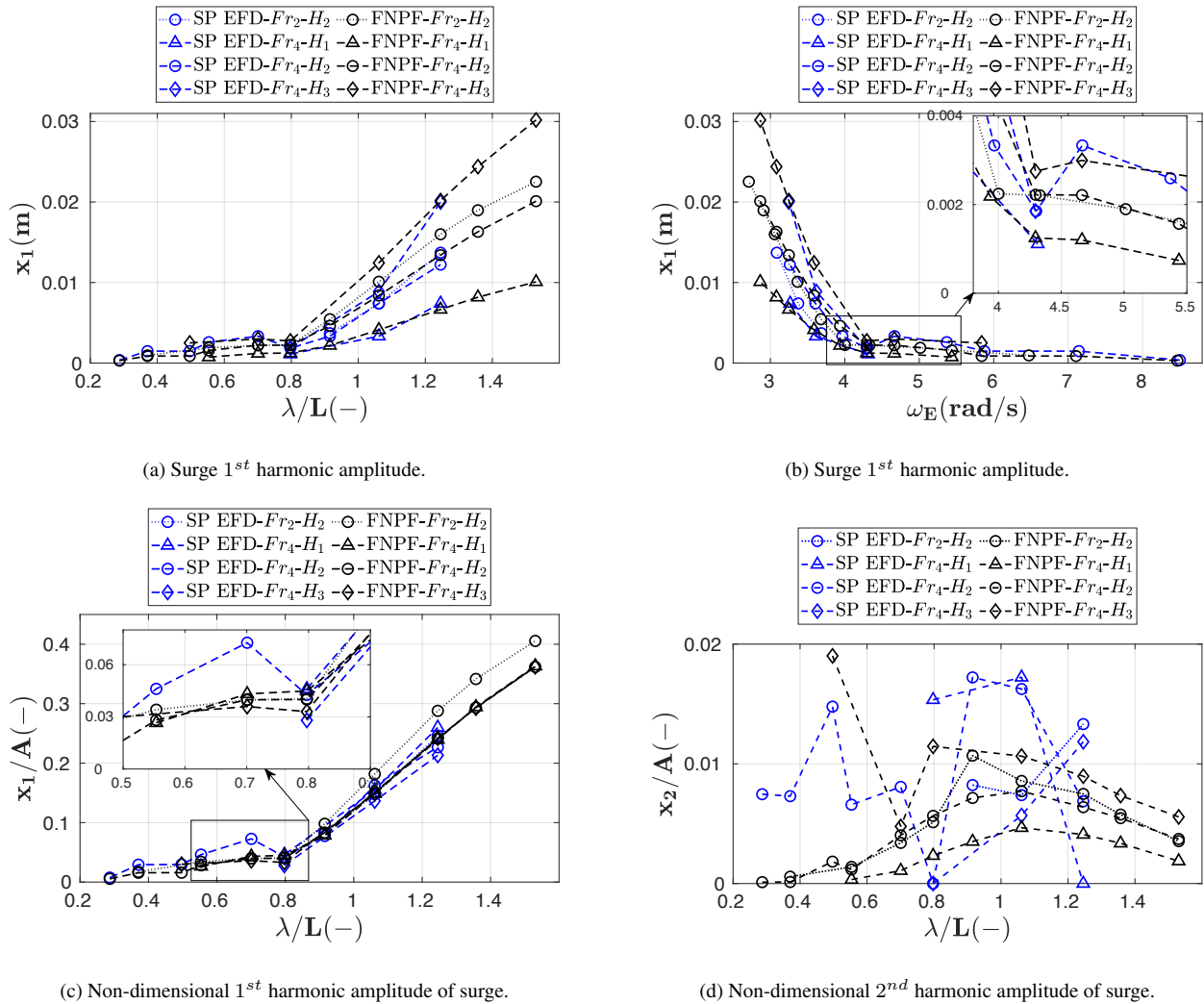


Figure 7: Comparison of the computed surge motion response with the measured values in regular head waves in ballast condition.

Pitch Motion The pitch motion response of the ship is shown in Figures 10 and 11 for the fully-loaded and ballast conditions, respectively. Global maxima for the 1st harmonic amplitudes of pitch motion are observed in the vicinity of $\lambda/L = 1.24$ in the fully-loaded condition and close to $\lambda/L = 1.35$ in the ballast condition, see Figures 10a and 11a. Presumably the maximum excitation pitch forces occur in the vicinity of these wave lengths and the combination with the radiation forces (considering the phase differences between them) yield the maxima in pitch motion. This hypothesis has also mentioned by Lewis (1989) and seen in the studies by Irvine et al. (2008), Sadat-Hosseini et al. (2013) and Simonsen et al. (2013) for different ship hulls that the maximum pitch excitation depends only on the ship length and the incident wave length which occurs in $\lambda/L \approx 1.33$. For the LDP vessel, in the vicinity of $\lambda/L = 1.24$, the cases with the same wave height and higher Froude numbers, exhibit larger θ_1 in the fully-loaded condition, see Figure 10a. Nevertheless, this trend is not seen in the ballast condition in Figure 11a, and θ_1 values near the global maxima are almost equal for H_2

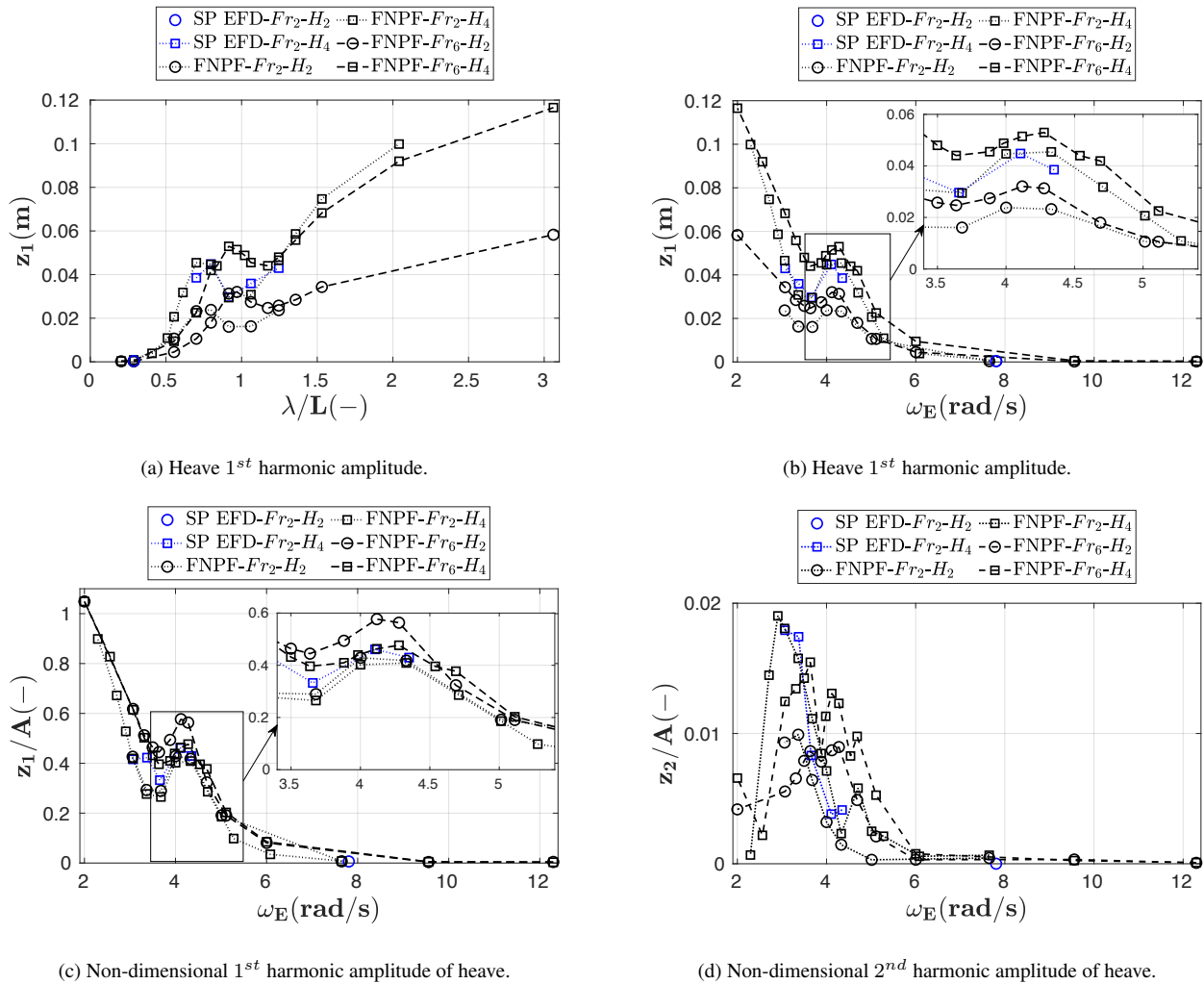


Figure 8: Comparison of the computed heave motion response with the measured values in regular head waves in fully-loaded condition.

at Fr_2 and Fr_4 .

There are small local maxima associated with resonance near the region in which the wave encounter frequency matches the pitch natural frequency in the ballast condition ($\omega_\theta \approx 5.34 \text{ rad/s}$), see Figure 11b. However, this trend is not seen in fully-loaded condition in Figure 10b for wave encounter frequencies close to $\omega_\theta \approx 4.44 \text{ rad/s}$. The reason might be that the wave excitation pitch forces continuously increase within that wave length range by increasing wave lengths, hence θ_1 increases accordingly and no local maximum occurs as the result of total wave forces in the fully-loaded condition. On the other hand, comparison of θ_1 values versus the non-dimensional wave lengths in Figures 10a and 11a reveals that these secondary local maxima appear in $\lambda/L = 0.55$ in both loading conditions. It is mentioned that the response of the ship in regular waves is formed as a result of combination of wave excitation and radiation forces amplitudes and phases. Since the radiation forces are expected to be relatively small in short waves, the effects of the wave excitation forces may probably

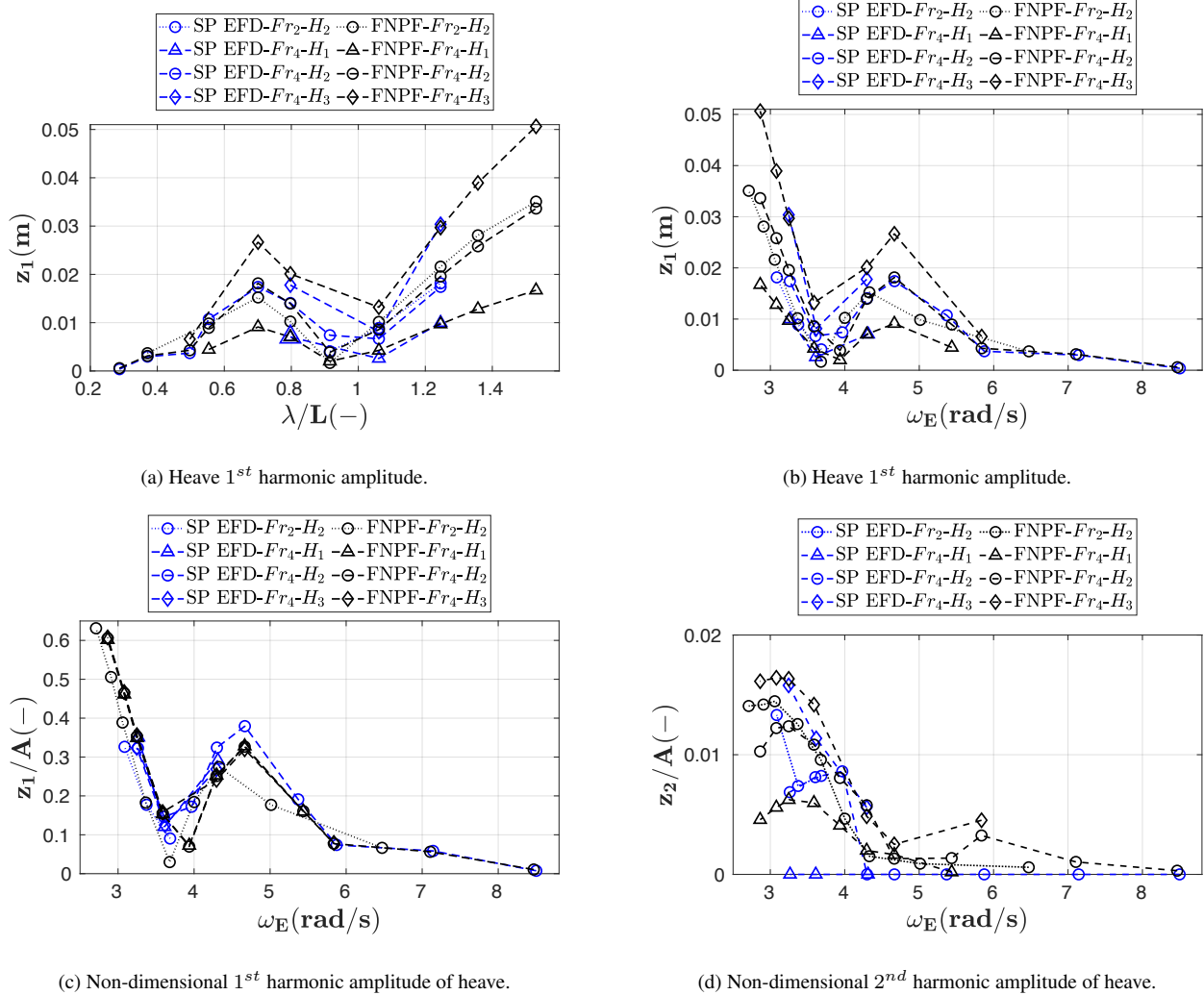


Figure 9: Comparison of the computed heave motion response with the measured values in regular head waves in ballast condition.

produced these secondary peaks. More studies on the pitch response of ships near $\lambda/L \approx 0.55$ are motivated. For the LDP vessel, these secondary peaks are comparatively larger in the ballast condition mainly due to the occurrence of the pitch resonance in the vicinity of $\lambda/L = 0.55$ at the studied Froude numbers.

The comparison of the non-dimensional 1st harmonic amplitude of pitch motion between the cases with the same Froude number and different wave heights clearly demonstrates an approximate linear relation between the pitch 1st harmonic amplitude and the wave slope kA , see Figures 10c and 11c. θ_1/kA near the maximum pitch excitation wave lengths are larger at the higher Froude numbers for the same wave height in the fully-loaded condition, however, almost equal in the ballast condition. The FNPF computed pitch motion response agrees well with the experimental data (in which the effects of actual measured incident wave amplitude is taken into consideration). Nonetheless, modest discrepancies of θ_1/kA are seen in the ballast condition in long

waves, see Figure 11c. These discrepancies are mainly under-predictions at Fr_4 and over-predictions at Fr_2 . The non-dimensional 2^{nd} harmonic amplitudes of pitch motion are shown in Figures 10d and 11d. Very small local peaks are seen near $\lambda/L \approx 1$ in both loading conditions. Although the 2^{nd} harmonic amplitudes of pitch motion have rather small values, very good predictions are obtained from the FNPF method as the trend of curves with respect to the wave length is similar to the trend of measured values.

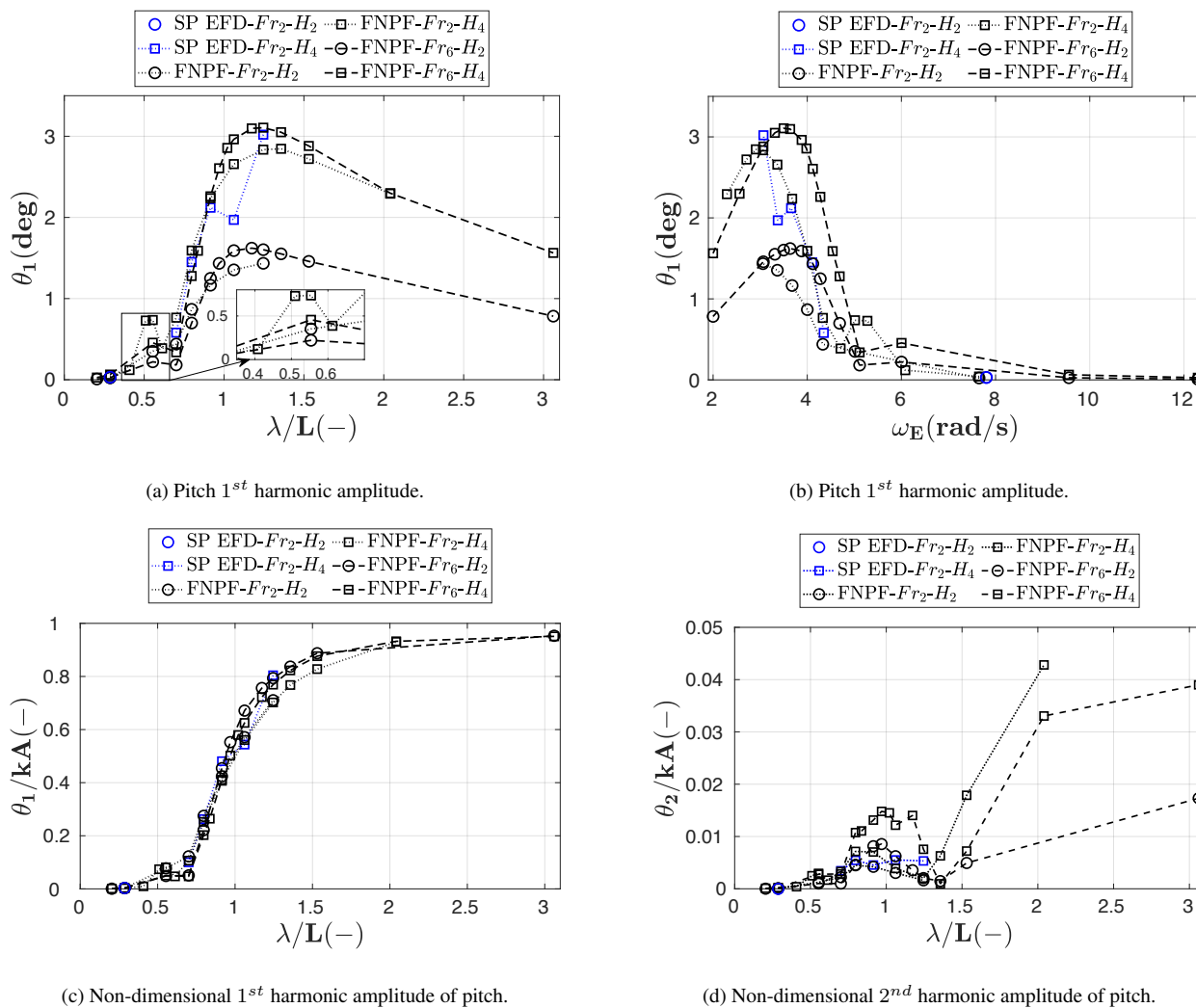
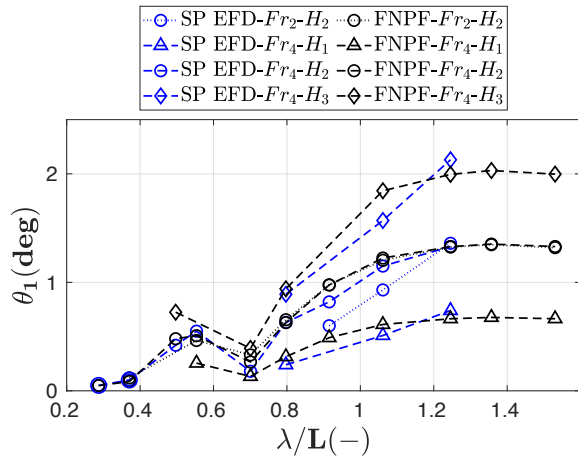
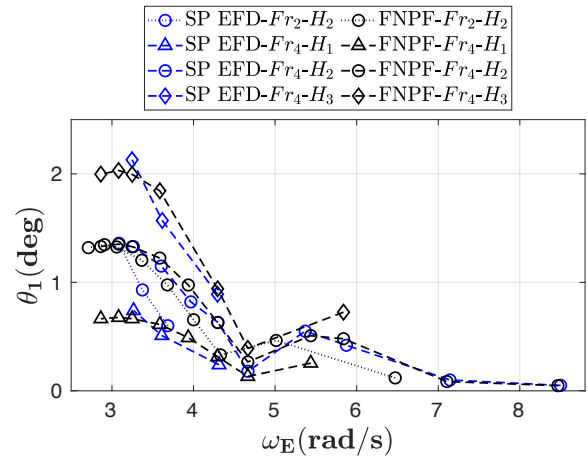


Figure 10: Comparison of the computed pitch motion response with the measured values in regular head waves in fully-loaded condition.

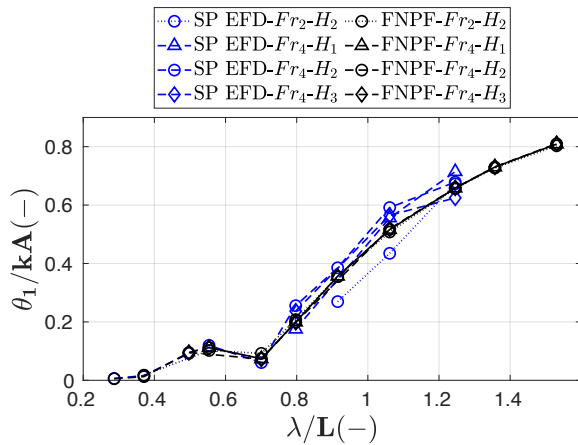
Based on the studied 1st harmonic amplitudes of different motions, it can be endorsed that the vessel in very long waves follows the water surface, as the surge, heave and pitch non-dimensional 1st harmonic amplitudes approach the value of 1 by increasing wave length. However, the overall behavior of the vessel over the wide range of wave lengths depends not only on the harmonic amplitudes of motions, but also on the harmonic phases of these motions. It is seen that the magnitudes of the surge motion responses are rather small, hence the



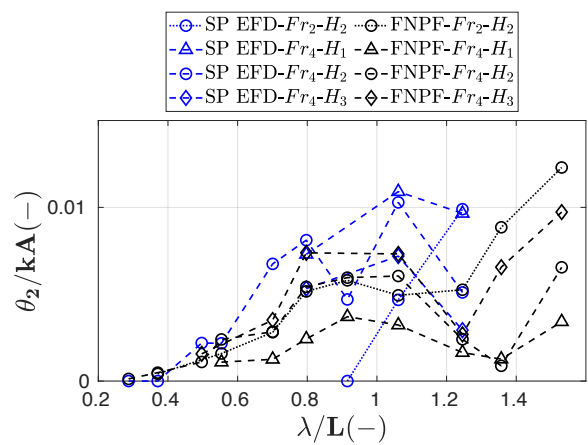
(a) Pitch 1st harmonic amplitude.



(b) Pitch 1st harmonic amplitude.



(c) Non-dimensional 1st harmonic amplitude of pitch.



(d) Non-dimensional 2nd harmonic amplitude of pitch.

Figure 11: Comparison of the computed pitch motion response with the measured values in regular head waves in ballast condition.

behavior of the vessel is mainly influenced by the heave and pitch motions in regular head waves. The first and second harmonic amplitude of these motions has been covered up to here. In the subsequent part the harmonic phase of these motions are presented to conclude the discussion.

Heave and Pitch Motions Phase Difference The 1st harmonic phase of pitch motion $\theta_{\varepsilon 1}$ is subtracted from the 1st harmonic phase of heave motion $z_{\varepsilon 1}$ for both loading conditions and the results are shown in Figure 12. The resulted phase difference curves for various conditions exhibit a quite similar trend when plotted against λ/L . The phase difference in very long waves approaches -90 deg confirming the behavior of the vessel in long waves in which the heave motion is synchronized with the wave motion near the COG and its phase goes to 0 deg while the pitch phase tends to 90 deg as the pitch response is in phase with the wave slope. A comparable trend in long waves is also seen by Sadat-Hosseini et al. (2013) and Simonsen et al. (2013) for KVLCC2 and

KCS vessels, respectively. The largest relative motions may occur when there are large amplitude motion responses together with a phase difference of $\pm 180 \text{ deg}$ or 0 deg . For the LDP vessel, the phase difference values are close to zero in $\lambda/L = 0.91$ at Fr_2 as well as $0.79 < \lambda/L < 1.02$ at Fr_6 in the fully-loaded condition. In ballast condition the phase difference for Fr_2-H_2 occurred in $\lambda/L = 0.91$. However, for other cases in the ballast condition, near-zero values of the phase difference are under-resolved in the simulations and additional wave lengths near $\lambda/L \approx 1$ are required to capture the condition with approximately zero phase difference. The trends of curves as well as the phase difference values computed in the FNPF method are comparable to that of self-propulsion model test data in both loading conditions.

The abrupt transition in the phase difference curves from high positive values to approximately -80 down to -90 deg in the vicinity of $\lambda/L = 0.55$ in the fully-loaded condition is an interesting feature, see Figure 12a. A similar behavior also can be seen in the ballast condition, however, since the ship responses are investigated only in a limited number of wave lengths near $\lambda/L = 0.55$, the trend of phase difference can not be precisely determined. It should be reminded that the secondary local maxima for θ_1 are also seen near such wave lengths, which encourages further investigations. Sadat-Hosseini et al. (2013) reported an abrupt jump of $\theta_{\varepsilon 1}$ of KVLCC2 around $\lambda/L = 0.7$. It should be noted that in the extreme short waves other harmonic amplitudes of motions have the same order of magnitude as the 1^{st} harmonic amplitude. Thus, the ship only oscillates with very small amplitudes around the calm water sinkage and trim values. The ship response in such conditions is particularly nonlinear with relatively small amplitudes, which makes the 1^{st} harmonic phase difference unimportant for determination of ship behavior. For instance, see Figure 12a for the abrupt transitions occurred in the shortest waves in the fully-loaded condition.

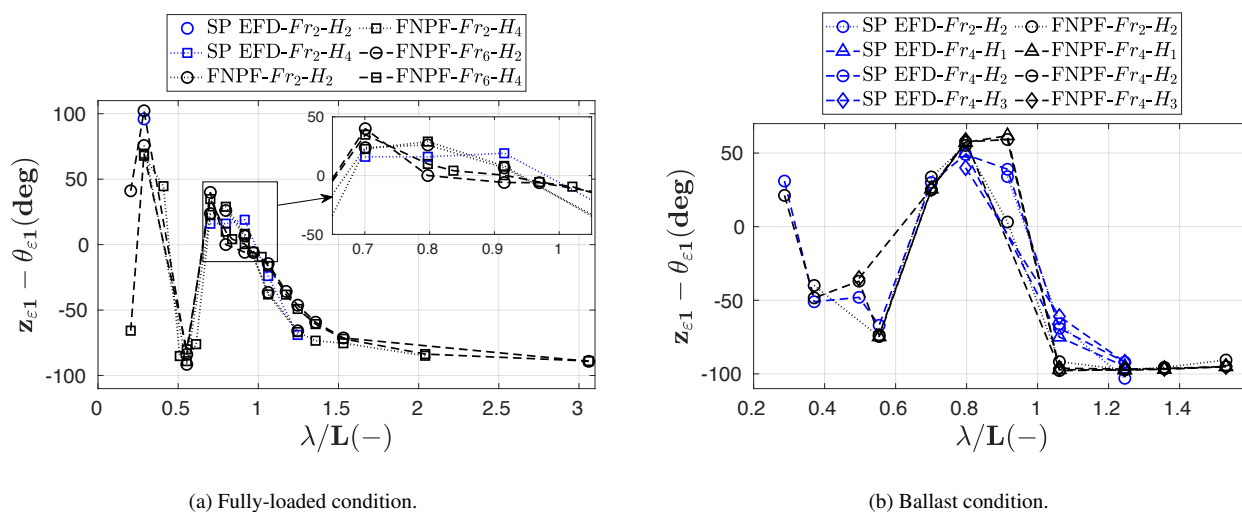


Figure 12: Comparison of the computed heave and pitch 1^{st} harmonic phase difference with the measured values in regular head waves.

Validation Error of Motions In order to present a quantitative analysis of errors associated with the FNPF method predictions compared to the experimental data, the averaged absolute errors are derived and shown in Table 4. First, the comparison errors in terms of percentage of the experimental data are calculated in the equivalent operational conditions shown in Table 3 for the dimensional and non-dimensional surge, heave and pitch 1st harmonic amplitudes. Then, the absolute error values $|E|$ are calculated and averaged $|\bar{E}|$ for the respective Froude numbers, wave heights and wave lengths in each loading condition for the mentioned responses. The averaged absolute errors reduce when the effects of actual incident wave heights measured in the model tests are taken into account, hence $|\bar{E}|$ for the non-dimensional 1st harmonic amplitudes are smaller than the dimensional 1st harmonic amplitude $|\bar{E}|$ for each motion response. The only exception is the heave motion response in the fully-loaded condition where the magnitude of the averaged absolute errors are relatively low. However, the effect of actual model speed in the self-propulsion model tests, which alters the wave encounter frequency, is not taken into consideration. The highest averaged absolute errors are seen for the surge motion response of the ship, mainly because that x_1 and x_1/A values are small, thereby small differences yield large errors.

Table 4: Averaged absolute errors of the FNPF method results in percentage of the experimental data for motion responses.

Loading Conditions	$ \bar{E} _{x_1}$ (%)	$ \bar{E} _{x_1/A}$ (%)	$ \bar{E} _{z_1}$ (%)	$ \bar{E} _{z_1/A}$ (%)	$ \bar{E} _{\theta_1}$ (%)	$ \bar{E} _{\theta_1/kA}$ (%)
Fully-loaded	56.6	47.2	7.1	13.4	18.5	9.9
Ballast	27.3	19.2	23.8	19.7	16.6	12.4

One possible source of discrepancy between the predicted motions by the FNPF method and model test data is the difference in the number of degrees of freedom between these methods and consequently, difference in the motion coupling. The model in the experiments was free in all six degrees of freedom that possibly has altered the ship responses in regular head waves. Moreover, a few other factors such as rudder or propeller existence may contribute to the discrepancy between the computed motions and the measured ones.

3.4.2 Resistance Responses

Wave Making Resistance The mean wave making resistance \bar{R}_W as well as the added wave resistance coefficient C_{AW} are shown for both loading conditions in Figures 13 and 17. The mean wave making resistance in self-propulsion model tests in regular head waves is deduced from the mean measured thrust based on Equation 5 assuming the same thrust deduction factor and frictional resistance as of calm water, see Section

3.2.1. Moreover, \bar{R}_F is computed for the mean attained speed \bar{V} and the thrust deduction factor at \bar{V} is interpolated from the calm water t_d at the speeds given in Table 2. The added wave resistance coefficient C_{AW} is computed from Equation 15, in which linear interpolation is used for calm water resistance R_W at the attained speed, see Section 3.2.4. It is worth mentioning that the negative calm water resistance values obtained from the simulations in ballast condition (see Section 3.3.1) are considered as zero in this equation. Moreover, in the calculation of C_{AW} , the considered wave amplitude A in FNPF computations is the theoretical 5th order Stokes wave amplitude, while in the experimental data A is derived from the wave height measurements based on the procedure explained in Section 3.2.4.

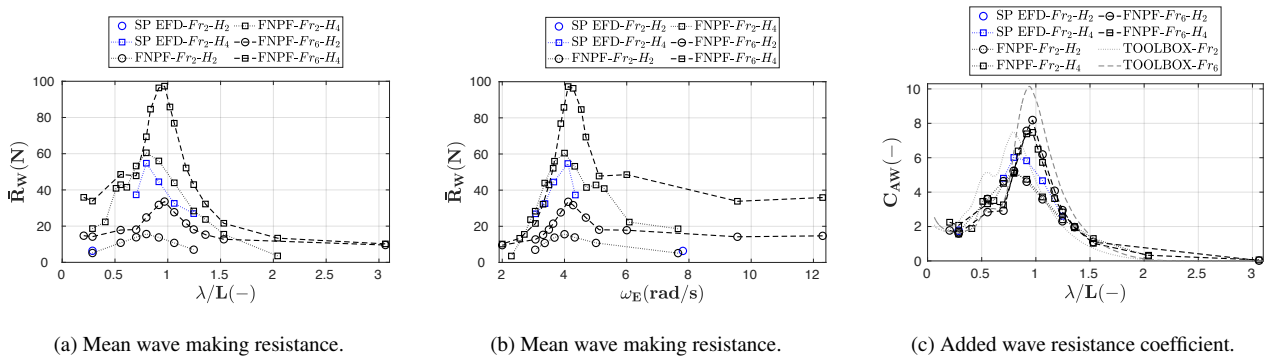


Figure 13: Comparison of the computed resistance response with the measured values in regular head waves in fully-loaded condition.

In the fully-loaded condition in Figure 13, the values of mean wave making resistance are larger for the higher encountered wave heights at the same Froude number. Moreover, the maximum value of \bar{R}_W at the same wave height increases by increasing Froude number while moving towards longer waves, see Figure 13a. The resistance peaks for the wave heights H_2 and H_4 occur in $\lambda/L = 0.79$ at Fr_2 as well as $\lambda/L = 0.97$ at Fr_6 . Comparison of \bar{R}_W versus ω_E in Figure 13b reveals that the main peaks of mean wave making resistance occur at the wave encounter frequencies which are rather close to the heave and pitch natural frequencies ($\omega_z \approx 4.22$ rad/s and $\omega_\theta \approx 4.44$ rad/s). In such conditions, θ_1 values are also relatively large (Figure 10b) and heave resonance yields a local maxima (Figure 8b). The 1st harmonic phase difference between heave and pitch motions in Figure 12a becomes approximately zero in the vicinity of $\lambda/L = 0.91$ at Fr_2 and in $0.79 < \lambda/L < 1.02$ at Fr_6 , which together with the heave and pitch motion responses produce large relative motions and hence large mean wave making resistance.

Another important aspect of the mean wave making resistance in Figure 13a is the existence of small secondary local peaks near $\lambda/L = 0.55$, except for Fr_2 - H_4 which is under-resolved in the simulations. Additional simulations with wave lengths in the vicinity of $\lambda/L = 0.55$ are required to capture a more accurate trend.

Although the heave and pitch motion responses are rather insignificant near such wavelength (shown in Figures 8a and 10a), small secondary local maxima are observed in the pitch 1st harmonic amplitudes of the vessel. Furthermore, the 1st harmonic phase difference between heave and pitch motions in the fully-loaded condition near $\lambda/L = 0.55$ abruptly changes to approximately -90 deg. Since the phase difference tends to -90 deg, the behavior of the vessel is mainly determined by either heave or pitch motion at a time, similar to the ship motions in very long waves. Therefore, due to the existence of the secondary local peaks of pitch motion, it might be concluded that the secondary peaks of the mean wave making resistance are mainly governed by the pitch motion responses of the vessel. The secondary peaks of \bar{R}_W , at the same Froude number, are more significant for H_4 in comparison to H_2 , similar to the respective θ_1 values near $\lambda/L = 0.55$.

The approximate linear relation of the added wave resistance to the wave amplitude squared has been discussed thoroughly in literature, for instance by Gerritsma and Beukelman (1972) and Block (1993). This can also be observed in Figure 13c as the cases with the same Froude number and different wave heights exhibit almost similar C_{AW} . Although the global trend of the added wave resistance is proportional to the wave amplitude squared, some conditions show a different trend. For instance, modest nonlinearities are seen in short waves as well as near the main peak of C_{AW} . Such nonlinear behavior is also reported for KVLCC2 by different authors, e.g. Yu et al. (2017), Lee et al. (2017), Lee et al. (2019) and Seo et al. (2020). Overall, the FNPF computed wave making resistance resembles well to the model test data and the wave length in which the main peak of C_{AW} occurs for Fr_2 - H_4 coincides in two methods. However, the computed and the measured C_{AW} values at the main peaks are different. Although in most of the studied wave lengths the measured mean wave making resistance is lower than the computed one, the relation between the measured and computed C_{AW} shows an opposite behavior when the effects of actual measured incident wave amplitude in model tests are taken into consideration. Interestingly, the TOOLBOX predicts the approximate wave lengths in which the peaks of added wave resistance coefficient occurs, however, it over-predicts the value of C_{AW} at both Froude numbers. The secondary peaks of added wave resistance coefficient near $\lambda/L = 0.55$ is also predicted by the TOOLBOX whereas the values of C_{AW} are over-predicted at Fr_2 and rather well predicted at Fr_6 compared to the FNPF results.

The computed harmonic amplitudes of wave making resistance by the FNPF method are shown in Figure 14 for the fully-loaded condition. The 1st harmonic amplitude of wave making resistance is the dominant component over the major range of wave lengths, except near $\lambda/L \approx 1$ in which the 2nd harmonic component is larger. R_{W1} is small in very short waves and has a large local peak around $\lambda/L \approx 0.55$, then its magnitude decreases

considerably around $\lambda/L \approx 1$ and again increases in long waves. R_{W1} for the cases with the same wave height and lower Froude number are lower before $\lambda/L < 1$ however larger when $\lambda/L > 1$. The second harmonic amplitude of wave making resistance R_{W2} is maximum in $\lambda/L = 0.97$ at Fr_6 (exactly the same wave length as of maximum \bar{R}_W) and in $\lambda/L = 0.91$ at Fr_2 (maximum of \bar{R}_W is in $\lambda/L = 0.79$) for both wave heights H_2 and H_4 . It should be noticed that the ship responses in $\lambda/L = 0.97$ at Fr_2 is under-resolved in the FNPF computations, see Table 3. The 3rd harmonic component is very small except in the vicinity of $\lambda/L = 0.83$ at Fr_6-H_4 . The wave making resistance response of the ship is mainly formed based on the different harmonic amplitudes of the wave making resistance together with the consideration of harmonic phases.

In order to have a clearer picture of the wave making resistance response of the ship, a selection of computed R_W time-series (the same time window in which the Fourier analysis is performed on) are shown in Figure 15 in the fully-loaded condition. The selected conditions are extracted for both of the studied wave heights in a short and a long wave length where the 1st harmonic amplitudes are larger than the higher harmonic amplitudes. Moreover, a wave length is selected near the region where the 1st harmonic amplitude is small and comparable to the higher harmonic amplitudes. The nonlinearities can also be observed in the time-series as the wave making resistance exhibits nonlinear behavior when the higher harmonics are significant.

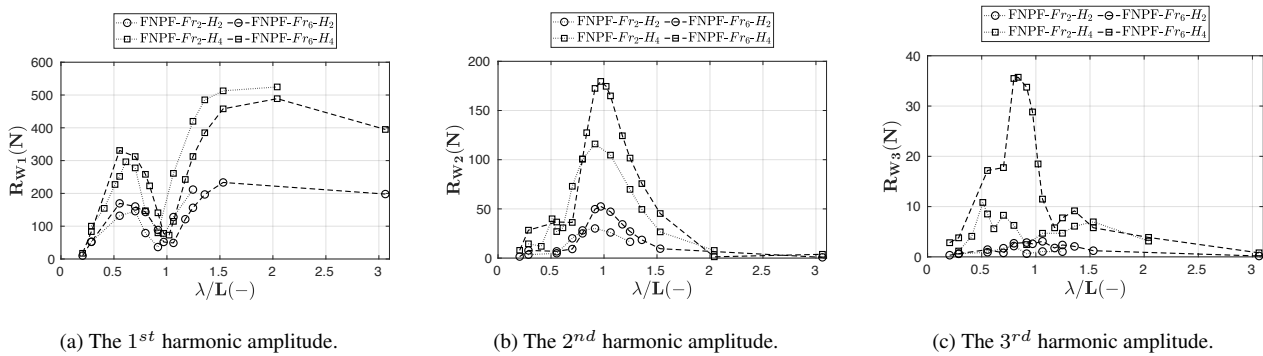


Figure 14: The harmonic amplitudes of wave making resistance in regular head waves in fully-loaded condition.

In Figure 16, the 1st and 2nd harmonic amplitudes of wave making resistance are non-dimensionalized by $\rho g B^2 A$ and $\rho g B^2 A^2 / L$, respectively. An approximately linear correlation between R_{W1} and the wave amplitude A is observed as the cases with the same Froude number and different wave heights have similar values in Figure 16a. $R_{W1} / \rho g B^2 A$ exhibit a considerably large peak within $0.50 < \lambda/L < 0.70$, which might be related to the secondary local maxima seen for θ_1 in the same wave length interval which is believed to be the cause of the secondary peak of C_{AW} . This might be the cause of the nonlinearities seen for the relation between the added wave resistance and wave amplitude squared in short waves. An approximately

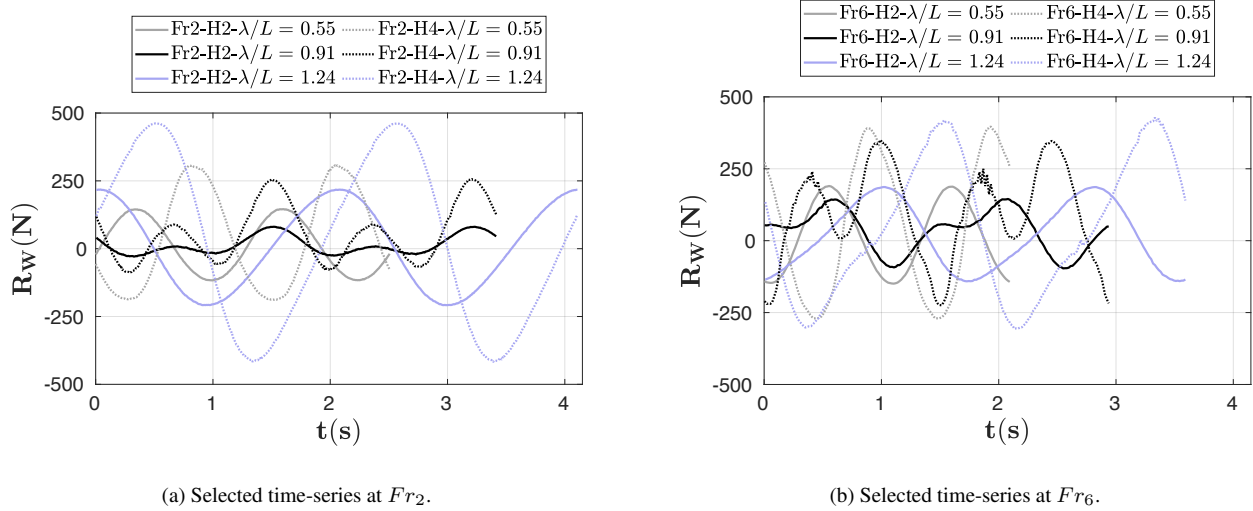


Figure 15: Wave making resistance time-series over two encountered wave periods in regular head waves in fully-loaded condition.

linear correlation between R_{W2} and the wave amplitude squared A^2 is seen in Figure 16b, except than the vicinity of $\lambda/L \approx 1$.

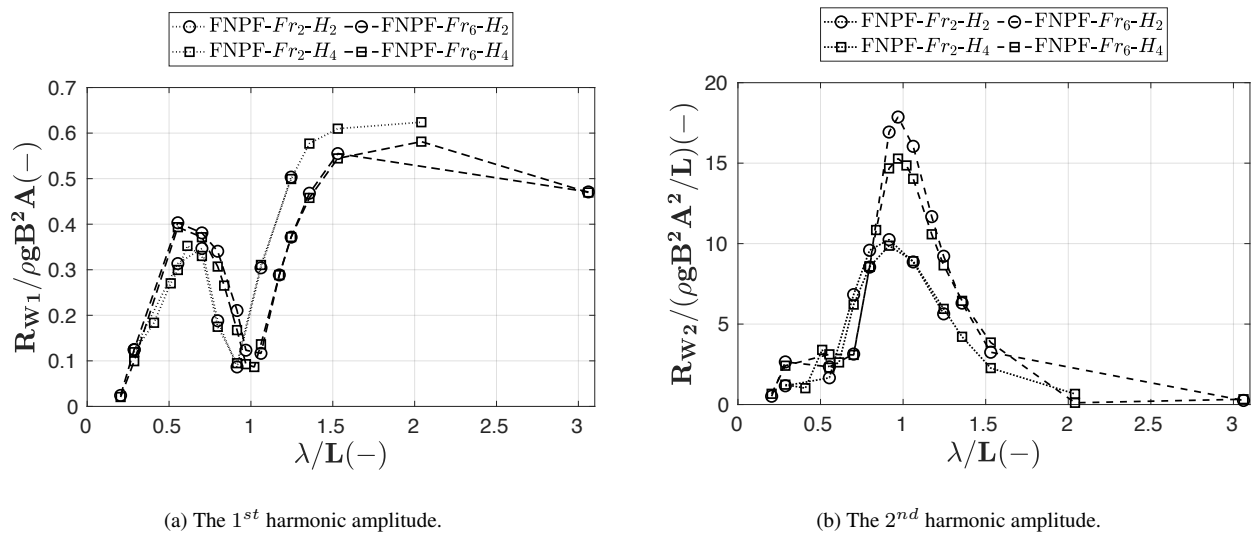


Figure 16: The non-dimensional harmonic amplitudes of wave making resistance in regular head waves in fully-loaded condition.

In the ballast condition in Figure 17, similar to the fully-loaded condition, the values of the mean wave making resistance are larger for the higher encountered wave heights at the same Froude number. Contrary to the fully-loaded condition, \bar{R}_W in the ballast condition does not vary significantly over the whole range of wave lengths and there are no dominant large peaks formed, see Figure 17a. Instead, there are two relatively small peaks near $\lambda/L = 0.49$ and $\lambda/L = 0.91$, while for Fr_2-H_2 in $\lambda/L = 0.49$ as well as Fr_4-H_3 in $\lambda/L = 0.91$ these peaks are under-resolved in the simulations. Although in the ballast condition local peaks are seen for z_1 and θ_1 in

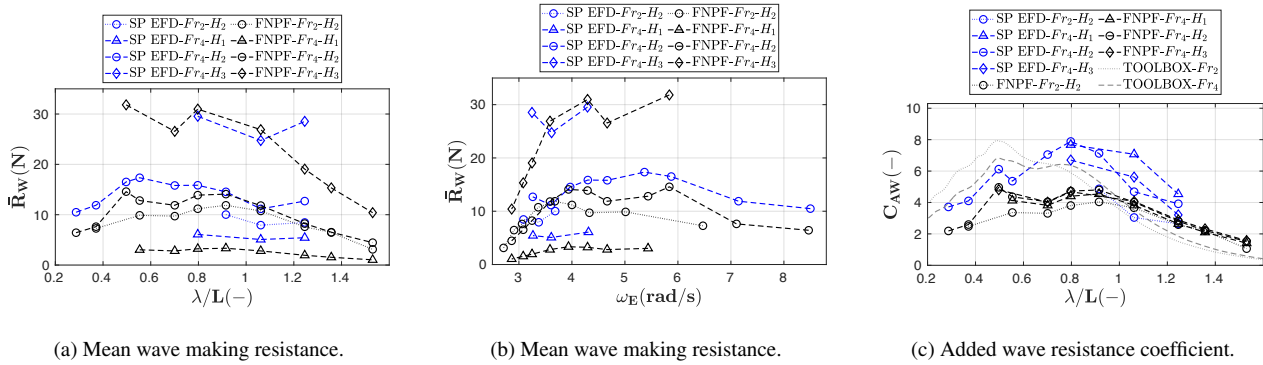


Figure 17: Comparison of the computed resistance response with the measured values in regular head waves in ballast condition.

the near resonance conditions, the peaks of \bar{R}_W do not coincide with the natural frequencies of heave and pitch motions. It should be noted that, the overall behavior of the hull is related not only to its motions amplitudes but also the phase differences of the motions. For instance, high value of \bar{R}_W at Fr_2-H_2 in $\lambda/L = 0.91$ might be due to the near zero 1st harmonic phase difference between heave and pitch motions and hence large relative motions in that wave length. It is seen that the near-zero phase difference for other conditions are under-resolved in the simulations. Due to the complexity of the motions amplitudes and phases in the ballast condition, it is hard to derive more solid statements regarding the relation of the mean wave making resistance to the motion responses.

Comparison of C_{AW} in the ballast condition reveals an approximate quadratic relation between wave amplitude and the added wave resistance in FNPF computations. Nevertheless, this dependency is not valid in the experimental data, as the measured C_{AW} values in different wave heights are scattered in long waves. The trend of computed \bar{R}_W is comparable to the experimental data in most of the wave lengths except from $\lambda/L = 1.06$ to $\lambda/L = 1.24$ in which the experimental resistance increases but the simulated one decreases, see Figure 17a. However, reduced C_{AW} in $\lambda/L = 1.24$ in Figure 17c reveals that the incident wave amplitude in those model tests were actually larger than the theoretical wave amplitudes, which explains the reason for larger measured mean wave making resistance relative to the simulated values, see Figure 17a. Although the trend of C_{AW} versus λ/L is rather similar in the FNPF computations and model test experiments, the computed added wave resistance coefficient is clearly under-predicted, except acceptable predictions for Fr_2-H_2 . One possible source of discrepancies might be related to the modest under-predictions of pitch motion at Fr_4 and small over-predictions at Fr_2 in Figure 11c. The C_{AW} results from the TOOLBOX also shows two peaks, while the peak in shorter waves is relatively higher at lower Froude number. It should be noted that the draft in the ballast condition in TOOLBOX is considered as the average draft between the fore and aft perpendiculars which does

not exactly resemble the ballast condition considered in the FNPF simulations and model test experiments, see Section 3.2.3.

The harmonic amplitudes of wave making resistance in the ballast condition are shown in Figure 18. The 1st harmonic amplitude of wave making resistance is the dominant component over the whole range of wave lengths, unlike the fully-loaded condition in which the 2nd harmonic amplitudes are dominant near $\lambda/L \approx 1$. R_{W3} is smaller than other harmonic amplitudes. R_{W1} is small in short waves up to $\lambda/L \approx 0.79$ and then it starts to increase in the longer waves. R_{W2} is large around $\lambda/L = 0.49$, where \bar{R}_W is also large in Figure 17a. Non-dimensional R_{W1} and R_{W2} are shown in Figure 20 where their relations with the wave amplitude is found to be similar to that of fully-loaded condition. It is interesting that the peaks of $R_{W2}/(\rho g B^2 A^2/L)$ occur in the same wave lengths as of peaks of C_{AW} in the ballast condition. A selection of R_W time-series in the ballast condition is shown in Figure 19. The nonlinear behavior of the wave making resistance time-series in $\lambda/L = 0.91$ at Fr_2 and in $\lambda/L = 1.06$ at Fr_4 can also be identified in the harmonic amplitudes of R_W in Figure 18.

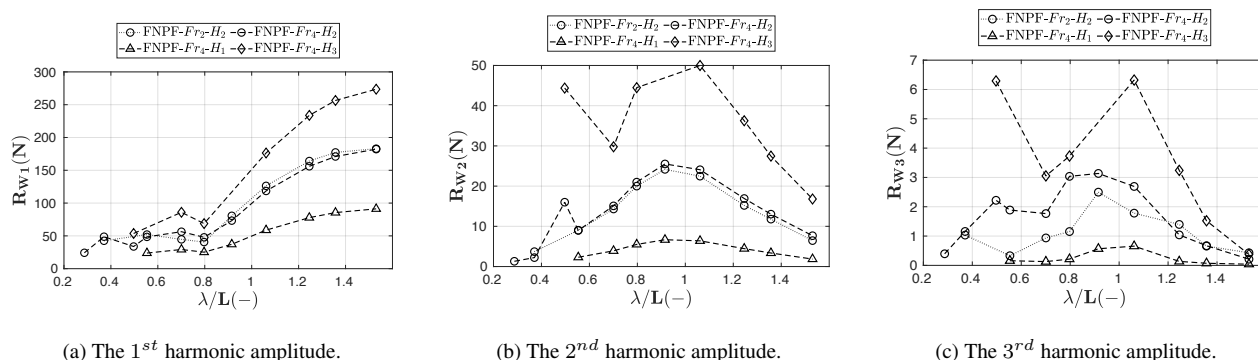


Figure 18: The harmonic amplitudes of wave making resistance in regular head waves in ballast condition.

Validation Error of Resistance The same procedure explained in Section 3.4.1 are used to calculate the averaged absolute errors of mean wave making resistance and added wave resistance coefficient in waves, see Table 5. Although the effect of actual incident wave height significantly reduced the averaged absolute error in the fully-loaded condition, $|\bar{E}|_{C_{AW}}$ is slightly increased in the ballast condition compared to the averaged absolute error of the mean wave making resistance.

Although the motions of the LDP vessel are predicted with a high level of accuracy through the potential flow computations, the accuracy of resistance predictions are arguable. C_{AW} in both loading conditions is mostly under-predicted compared to the experimental data. It should be kept in mind that the model tests have been

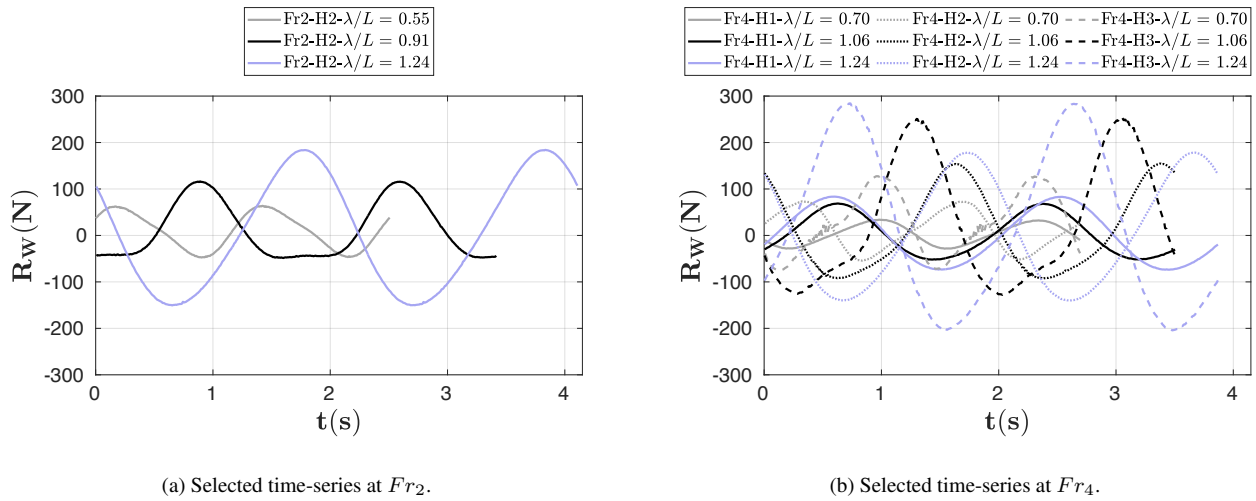


Figure 19: Wave making resistance time-series over two encountered wave periods in regular head waves in ballast condition.

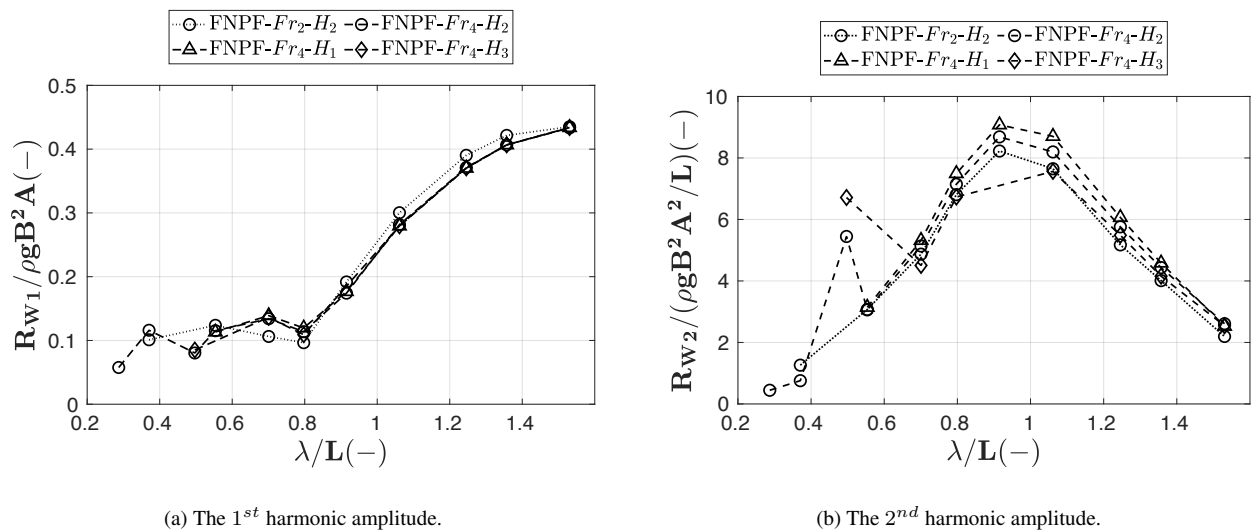


Figure 20: The non-dimensional harmonic amplitudes of wave making resistance in regular head waves in ballast condition.

carried out in free-sailing self-propulsion mode while the FNPF computations were performed for the bare hull in 3DOF. One source of discrepancy would be the other degrees of freedom present in the model tests. Valanto and Hong (2017) also mentioned that all motion responses have an effect on the wave added resistance of a cruise ship. Another source of discrepancy might be related to the propeller ventilation. Although the LDP was initially expected to undergo severe ventilation, it was found during the tests that the “tunnel-shaped” aft configuration is very effective in keeping the propeller submerged. Propeller ventilation was observed in some operational conditions mostly in the cases with wave heights of H_3 or H_4 . Although, the thrust and torque measurements showed relatively little sensitivity to occurrences of ventilation, minor effects could be anticipated on the results. It should be noticed that the interactions between the incoming waves, hull and

Table 5: Averaged absolute errors of the FNPF method results in percentage of the experimental data for resistance responses.

Loading Conditions	$ \bar{E} _{\bar{R}_W}$ (%)	$ \bar{E} _{C_{AW}}$ (%)
Fully-loaded	23.1	12.0
Ballast	25.6	28.3

propulsion system of the ship may strongly influence its performance in waves. Therefore, another source of discrepancy may be related to the considered assumption of similar R_F and t_d for the ship operating in regular head waves and in calm water.

Frictional Resistance In order to examine the assumption on the frictional resistance, \bar{R}_F in waves is calculated in the FNPF computations and compared with the respective calm water R_F in Figure 21. From simulations, at each time step the instantaneous velocity and wetted surface area are known. First, the instantaneous Reynolds number is computed assuming constant L . Then, the instantaneous C_F from the ITTC-57 model-ship correlation line in Equation 3 is calculated. Finally, by using the instantaneous wetted surface area, the instantaneous R_F is calculated from Equation 2. Similar to other responses, Fourier analysis on the R_F time-series is performed over the last two encountered wave periods when the simulations are converged. The change of mean frictional resistance in waves \bar{R}_F is then computed in terms of percentage of the calm water frictional resistance R_F at each respective Froude number, see Figure 21. It can be seen that the mean frictional resistance is very similar to the calm water frictional resistance over the whole ranges of wave lengths in both loading conditions, as the change of frictional resistance in regular waves remains less than 2% of the calm water value. It should be noticed that other viscous effects such as periodic flow separations at the stern, splashes, bow and stern slamming and green water on deck are not taken into account and the frictional resistance coefficient is estimated from the ITTC-57 model-ship correlation line in Equation 3. Higher fidelity viscous flow CFD simulations are needed for investigation of the aforementioned effects.

The change of wetted surface area in time in regular head waves exhibit a periodic behavior with a frequency equal to the wave encounter frequency. Therefore, Fourier analysis is performed on the time-series of wetted surface area captured in the FNPF simulations. The 0^{th} and the 1^{st} harmonic amplitudes are the dominant components, whereas higher harmonic components are negligible. The change of mean wetted surface area \bar{S} in waves relative to the calm water wetted surface area S at each respective Froude number is shown in Figure 22. Change of the mean wetted surface area remains approximately less than 1% of the calm water S

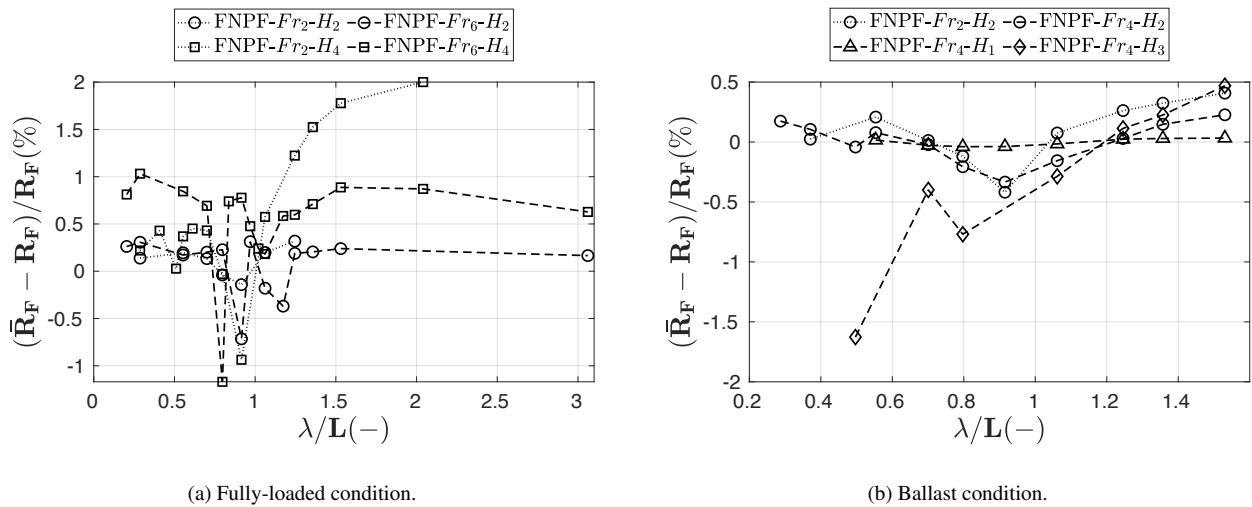


Figure 21: Change of \bar{R}_F in waves in terms of percentage of its calm water value.

over the major part of the studied wave lengths in both loading conditions. In very long waves the values of \bar{S} approaches the calm water wetted surface area as the vessel follows the water surface. Moreover, as shown in Figure 23, the first harmonic amplitude of wetted surface area S_1 in regular head waves are found to have an approximately linear relation with respect to wave amplitude in the cases with the same Froude number.

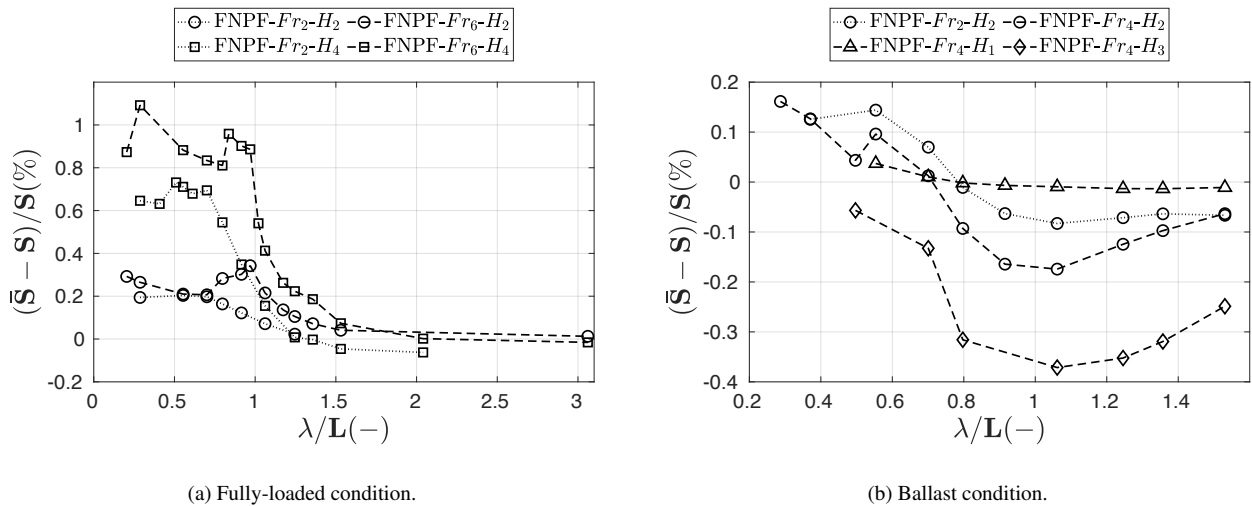


Figure 22: Change of the mean wetted surface area in regular head waves in terms of the percentage of its calm water value.

3.5 Conclusions

In this study, the hydrodynamic performance of a general cargo ship was investigated in terms of resistance and motions responses in calm water as well as in regular head waves. Two loading conditions were considered, namely, fully-loaded and ballast. A Fully Nonlinear Potential Flow (FNPf) panel method was used in

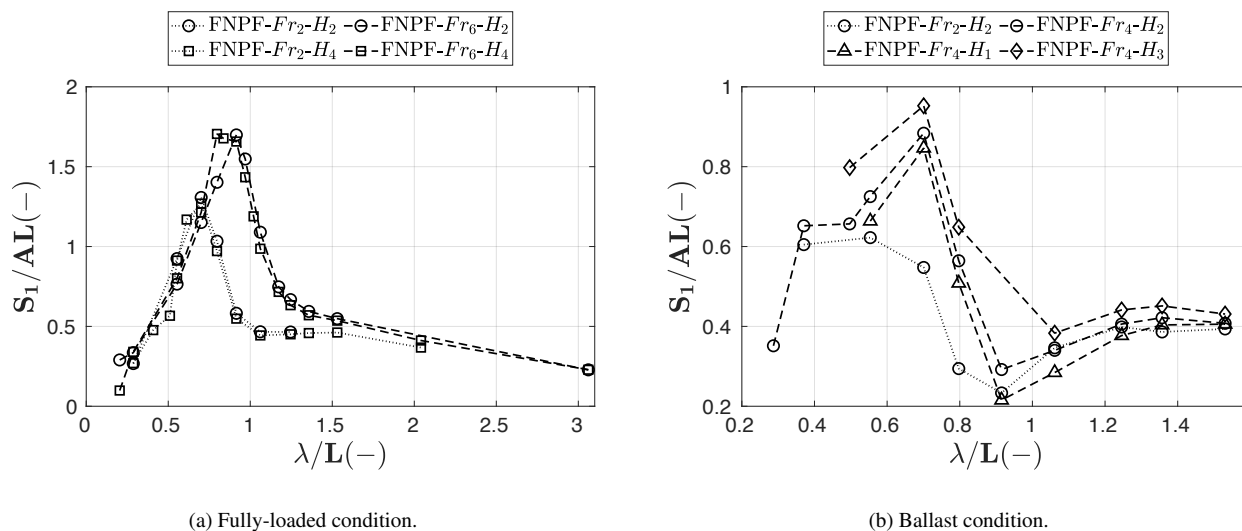


Figure 23: The 1st harmonic amplitude of change of wetted surface area in regular head waves.

order to predict the performance of the vessel in a wide range of operational conditions (loading conditions, Froude numbers, wave heights and wave lengths). Several computational settings (e.g., computational domain dimensions, hull and free surface discretization and time step size) in the FNPF solver were specified in order to attain a high level of computational efficiency with respect to cost and accuracy. The computational results were compared against model test data.

Our investigations in calm water at different Froude numbers include resistance simulations as well as free decay heave and pitch simulations (for obtaining natural periods of these motions) in various degrees of freedom. The computed wave making resistance, sinkage and trim by the FNPF method in calm water were in a rather good agreement with the measured data, except modest under-predictions of wave making resistance seen in the ballast condition at lower Froude numbers.

The 1st harmonic amplitudes of motions were the dominating components in the Fourier analysis of the motions responses in waves. The magnitudes of the 1st harmonic amplitudes of surge motion x_1 were rather small except in very long waves. Further investigations are motivated on the very small local peaks seen in x_1 near $\lambda/L = 0.7$, in which the wave excitation surge forces associated with the ratio between the length of parallel mid-body and the incident wave length can be examined. In both loading conditions, the 1st harmonic amplitudes of heave motion z_1 exhibited local maxima near the heave resonance conditions, i.e., when the encounter wave frequency was close to the heave natural frequency. The heave resonances in the ballast condition were more intense resulting in prominent local maxima. Small local maxima near the resonance conditions were seen in the 1st harmonic amplitudes of pitch motion θ_1 solely in the ballast condition, whereas in the fully-

loaded condition, the increasing pitch excitation wave forces near resonance conditions were believed to be the main reason for the absence of local maxima. On the other hand, θ_1 exhibited large peaks resulted from high excitation wave forces near $\lambda/L = 1.24$ and $\lambda/L = 1.35$ in the fully-loaded and ballast conditions, respectively. Furthermore, secondary local maxima for θ_1 were seen near $\lambda/L = 0.55$ in both loading conditions. These local peaks in the ballast condition coincided with the pitch resonance conditions resulting in considerable pitch 1st harmonic amplitudes. The 2nd harmonic amplitudes of motions are relatively lower than the 1st harmonic amplitudes except where both components are small and the ship motion responses are nonlinear with very small magnitudes.

The 1st harmonic phase differences between heave and pitch motions $z_{\epsilon 1} - \theta_{\epsilon 1}$ versus wave length exhibited rather similar trends in different operational conditions. The phase differences in very long waves approached -90 deg confirming the behavior of the vessel in long waves. In long waves, the heave motion was synchronized with the wave motion near the center of gravity (COG) and its phase converged to 0 deg , while the pitch phase tended to 90 deg , since the pitch response was in phase with the wave slope. Interesting abrupt transitions were seen in the phase difference curves near $\lambda/L = 0.55$. Overall, the predicted motions responses by the current FNPF method in regular head waves were in good agreement with the experimental data.

Another aspect investigated in this study was the 0th, 1st and 2nd harmonic amplitudes of the wave making resistance as well as the added wave resistance coefficients C_{AW} in different operational conditions. The 0th harmonic amplitude (mean value) of the wave making resistance \bar{R}_W exhibited large peaks in the fully-loaded condition close to the heave and pitch natural frequencies, while the variation of \bar{R}_W in the ballast condition stayed insignificant over the major range of the studied wave encounter frequencies. Interestingly, two peaks in each loading condition were seen for the added wave resistance coefficient. Although in the fully-loaded condition one of the peaks in the longer waves was dominating, the peaks were rather equal in size in the ballast condition. The main peaks of C_{AW} in the fully-loaded condition were larger for the higher Froude numbers and moved towards longer waves. The secondary peaks of C_{AW} were seen in short waves near $\lambda/L = 0.55$ in the fully-loaded condition and near $\lambda/L = 0.49$ in the ballast condition. It is believed that these secondary peaks were related to the secondary peaks of θ_1 as well as the abrupt transitions of the 1st harmonic phase difference between heave and pitch motions observed near such wave lengths. Further investigations for different hull types and operational conditions are recommended for better understanding of the behavior of ships near $\lambda/L \approx 0.5$.

C_{AW} at each Froude number in both loading conditions indicated approximate linear relation between the added

wave making resistance and the wave amplitude squared in the FNPF computational results, except in relatively short waves and near the peaks. However, this quadratic wave amplitude dependency of added wave resistance was not well identified from the experimental data in the ballast condition. Moreover, from the potential flow computations in both loading conditions, approximately linear correlations were observed for the 1st and 2nd harmonic amplitudes of the wave making resistance (R_{W1} and R_{W2}) against the wave amplitude and the wave amplitude squared, respectively.

Although the computed motions in the FNPF method were comparable to the measurements, the resistance results were arguably less accurate in some conditions. The averaged absolute error of FNPF computational results in terms of percentage of the experimental values in both loading conditions for surge, heave and pitch 1st harmonic amplitudes were 34.6%, 19.6% and 17.1%, respectively. When the effects of actual measured wave height in the model tests were taken into account, the average absolute error of the non-dimensional 1st harmonic amplitudes of surge, heave and pitch motions reduced to 26.2%, 18.1% and 11.8%, respectively. On the other hand, the averaged absolute errors associated with the mean wave making resistance and added wave resistance coefficient (considering the actual incident wave height in the experiments) were found to be 25.0% and 24.3%, respectively. Generally, numerical errors in conjunction with the discretization errors as well as the potential flow approximations and the use of empirical formulas, such as ITTC-57 model-ship correlation line, are the main sources which contribute to discrepancy between the computed and the measured results. Moreover, the uncertainty related to the experimental data as well as the differences between the experimental and numerical setups (6DOF self-propelled against 3DOF bare hull) in this study should not be forgotten. The frictional resistance and thrust deduction factor in waves were assumed to be equal to those of calm water. However, the interaction effects between waves, hull and propulsion system may dispute the validity of these assumptions. Based on a simple approximations in the FNPF solver, the change of frictional resistance in presence of waves was found to be less than 2% of the respective calm water values. Supplementary investigations on the change of thrust deduction factor as well as frictional resistance in the presence of waves by higher fidelity viscous flow methods are encouraged.

The FNPF computational cost for each simulation was approximately 20-80 core-hours which lies between the computational cost required by lower fidelity methods (often with lower accuracy) such as methods based on Strip Theory and higher fidelity methods such as viscous flow solvers. Although the FNPF computational cost is considerably lower than the cost of higher fidelity methods, yet the results are in a good agreement with the experimental data. Therefore, the utilization of the FNPF methods in prediction of the overall performance of

ships in regular head waves is found to be computationally efficient and cost-effective.

4 Viscous Flow Simulation of Ship Hydrodynamics in Waves

Since calm water is rather an exception at an actual sea, optimizing propulsive efficiency of ships operating in more realistic environmental conditions than calm water has been gaining more attention recently. The effects of waves on propeller performance have been investigated by different researchers such as Taskar et al. (2016a) who studied different influencing factors in terms of cavitation, pressure pulses and efficiency on propeller performance of KVLCC2. Since excessive wake variation in waves may have a significant impact on the propeller performance, it is important to study dynamics of the wake field for ships operating in waves.

Although the propeller designers consider experienced-based margins for propellers operating in waves and off-design conditions, the knowledge of the wake field at different wave conditions for each specific hull could be beneficial in designing more efficient propeller. In this study, a general cargo vessel incorporating a Large Diameter Propeller (LDP) with a very small tip clearance is considered. In an earlier investigation, the authors of the current work have carried out a study, Irannezhad et al. (2019), on the propeller emergence risk assessment of the LDP vessel employing a potential flow panel code, SHIPFLOW Motions, as well as a viscous flow solver, STAR-CCM+. The aim of this part of the work is to first validate the LDP vessel computed heave and pitch motions as well as its resistance due to regular head waves in model scale against the experimental data, then to analyze the time-varying wake field and compare it in different wave conditions in the viscous flow solver. The propeller is not modeled in the simulations.

4.1 Vessel geometry and conditions

An overview of the LDP vessel geometry with a tunnel-shaped aft design meant to accommodate an LDP is shown in Fig. 24 together with the ship-fixed coordinate system at the vessel Center Of Gravity (COG). A simple shaft connects the vessel bare hull to an appended asymmetric rudder. Although the LDP is not modeled in the simulations, its conceptual geometry is represented in Fig. 24. A point probe at the position of the LDP blade tip near the propeller/hull clearance is specified in order to characterize the propeller emergence in the absence of propeller in the simulations. The LDP vessel main particulars in model-scale, its speed as well as the corresponding Froude number are listed in Table 6.

Table 6: The model-scale LDP vessel main particulars and conditions (scale factor = 27).

Particular	\approx Value	Unit	Denotation
L_{pp}	7.95	[m]	Length Between Perpendiculars
LOS	8.11	[m]	Length Overall Submerged
B	0.88	[m]	Breadth at mid-ship
T_A	0.296	[m]	Draft at Aft Perpendicular
T_F	0.296	[m]	Draft at Fore Perpendicular
Δ	1740	[kg]	Mass Displacement
V	0.89	$[\frac{m}{s}]$	Model Speed
Fr	0.10	[-]	Froude Number
Re	7.1E6	[-]	Reynolds Number



Figure 24: LDP vessel geometry, point probe and ship-fixed coordinate system at COG.

The model-scale LDP vessel appended with a rudder and a shaft, free to heave and pitch operating in fresh water with the density of $\rho = 998.3 \frac{kg}{m^3}$ is used within the numerical investigations. The simulations are performed in calm water and in the 5th order Stokes regular head waves ($\mu = 180^\circ$) in deep water as listed in Table 7. On the other hand, the LDP vessel model-tests were conducted in free-running self-propulsion mode by Maritime Research Institute Netherlands (MARIN). Fast Fourier Transform (FFT) analysis is used in order to post-process the experimental and numerical data.

Table 7: Environmental conditions of the studied cases.

Case no.	Cond.	$\approx H$ [m]	$\approx \lambda$ [m]	$\approx \frac{\lambda}{LOS}$ [-]	$\approx \text{Steepness} = \frac{H}{\lambda}$ [-]	$\approx \omega_e$ [$\frac{rad}{s}$]	$\approx T_e$ [s]
1	Calm	-	-	-	-	-	-
2	Wave	0.22	5.57	0.68	0.039	4.33	1.45
3	Wave	0.22	7.27	0.89	0.030	3.68	1.70

The total resistance R_T in self-propulsion model tests is estimated based on the mean measured thrust \bar{T} and the given calm water thrust deduction factor of $t_d = 0.159$ at Froude number 0.10, see Eq. 18. It is assumed that the thrust deduction factor in waves is equal to that of calm water, t_d .

$$R_T = (1 - t_d) \times \bar{T}. \quad (18)$$

4.2 Numerical modeling

The CFD simulations are performed using an URANS approach. A second order spacial discretization scheme is used. In order to simulate the vessel motions, the Dynamic Fluid Body Interaction (DFBI) module is used. The DFBI Rotation and Translation model is used in order to enable the RANS solver to compute the vessel motions from the exciting fluid forces and moments as well as the gravity force. The Planar Motion Carriage mechanism is used within the DFBI Rotation and Translation model, in order to simulate the hull free to heave and pitch (2 degrees of freedom) while it is translating with a prescribed constant speed (ship forward speed V) in the longitudinal direction in the earth-fixed coordinate system. In order to achieve a robust simulation setup for wave propagation in STAR-CCM+, the best practice provided by M (2017) is complied. The aim is to minimize the wave propagation simulation issues, such as amplitude reduction and period change during propagation, disturbances (wiggles) on the free-surface and reflection at boundaries. The Volume of Fluid (VOF) multiphase model is used as the free-surface capturing technique. The High-Resolution Interface Capturing (HRIC) scheme by Muzaferija and Peri'c (1999) is used in VOF simulations to maintain a sharp interface between the incompressible fluid phases.

Mesh generation was performed using the automatic mesh generation tool in STAR-CCM+. The trimmed hexahedral meshes with local refinements near the free-surface as well as near the hull together with prism

layers along the hull surface are used. Overset method consisting a moving overset region and a stationary background region with specific treatment of cell sizes near the overlapping region is used to discretize the computational domain. The prism layers are placed in such a way that the non-dimensional wall distance y^+ remains above 30 over the major part of the hull surface during the simulation, hence wall functions utilization. An overview of the background mesh is shown in Fig. 25 in which the applied boundary conditions is also given. The pressure outlet boundary condition for simulation in calm water is moved from the top boundary to the outlet boundary. Due to the asymmetric geometry of the rudder, no symmetry plane is considered and both side boundaries are given as velocity inlets. For simulations in waves, the wave forcing capability is applied to all of the vertical boundaries in order to force the solution of the discretized Navier-Stokes equations towards the theoretical 5th order Stokes wave solution over a distance equal to Length Overall Submerged (LOS) from the boundaries. For simulation in calm water, the wave damping capability is used in all of the vertical boundaries in order to minimize the wave reflection from the boundaries. The Standard Low-Re $k - \varepsilon$ turbulence model and the Realizable $k - \varepsilon$ turbulence model together with all y^+ wall treatment are used for simulations in waves and calm water respectively. An implicit unsteady solver with a second order temporal discretizational scheme (time-step of 0.003 s) for simulation in waves and a first order temporal discretizational scheme (time-step of 0.02 s) for simulation in calm water is used. The chosen time-step also fulfills the ITTC (2011) recommended criteria of at least 100 time-steps per encountered wave period. Last but not least, ten and forty maximum number of inner iterations for each unsteady time-step is considered in simulations in waves and calm water respectively.

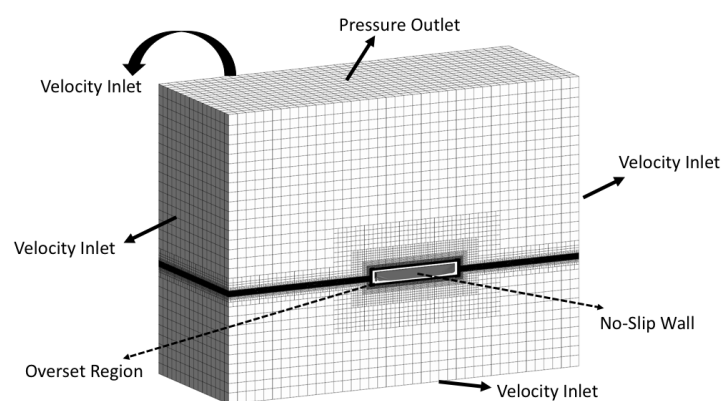


Figure 25: An overview of the background mesh and the applied boundary conditions.

Table 8: Number of cells in each region.

Cond.	Background	Overset	Total
Calm	5.8 M	2.3 M	8.1 M
Wave	13.5 M	4.1 M	17.6 M

4.3 Resistance and motions validation

Due to a very small Froude number, the dynamic sinkage and trim as well as the wave making resistance in calm water attain very small values. The self-propelled model test sinkage, trim and total resistance are -0.003 [m], 0.017 [deg] and 15.8 [N], respectively, while the CFD results are -0.002 [m], 0.114 [deg] and 14.6 [N]. Positive sinkage and heave (R3) defined as COG moves upward and positive trim and pitch (R5) are defined as bow moves downward. The 0^{th} harmonic amplitudes of motions in simulations in waves are approximately similar and relatively small. Nevertheless, the 1^{st} harmonic amplitudes of heave and pitch motions, shown in Fig. 26, are the dominating components while higher order components are close to zero. The large amplitude heave response in Case 2 might be due to the near heave resonance conditions. The deviation errors of the 1^{st} harmonic amplitudes of motions and the 0^{th} harmonic amplitudes of resistance from the experimental data are presented on top of each bar in Fig. 26e and 26f. In general, a good agreement is seen between CFD and EFD data.

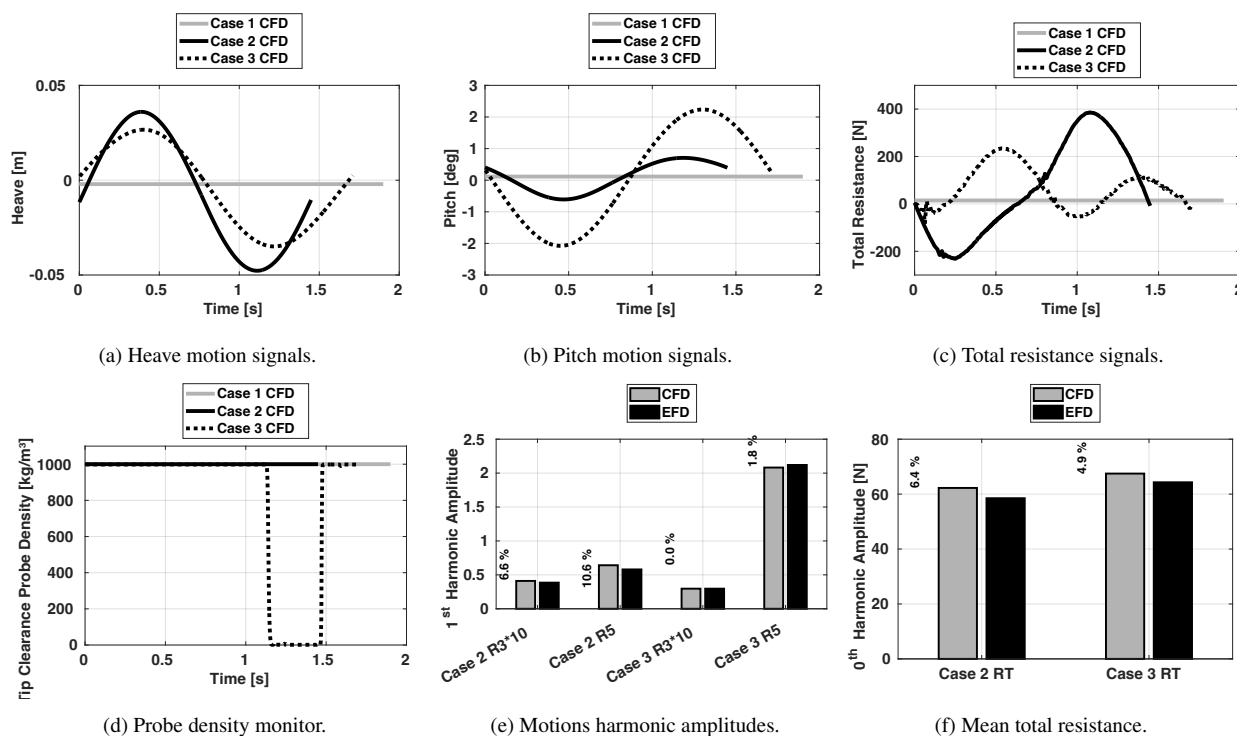


Figure 26: The LDP vessel responses during one encountered wave period.

4.4 Propeller wake investigations

In this section the nominal wake variation in waves and in calm water is investigated for the LDP vessel. The wake has been studied on a virtual disk located at the propeller center and it is moving with the hull during the motion responses. The disk radius is equal to the propeller radius ≈ 0.13 m. The propeller disk is divided into 11 surfaces in radial direction, with the first surface starts at the shaft edge to a radius of $\Delta r_1 = 0.03m$ and the remaining 10 surfaces with the radius steps of $\Delta r_{2...11} = 0.01m$ to the propeller tip. The disk surface centers are also derived. The mean value of the surface averaged axial and radial velocity components during one encountered wave period is shown in the Fig. 30b and 30c at each surface center radius. The surface averaged calm water wake fraction as well as the surface averaged wake fraction variation during one encounter wave period for simulations in waves are shown in Fig. 30a. Significant wake variation in waves in comparison to calm water wake is seen. The computed values of the mean surface averaged wake fraction for Case 2 and Case 3 are approximately similar to the calm water value; however, a different distribution of the axial and radial velocity components are observed, see Fig. 30b and 30c. The sudden change of wake fraction in Case 3 between 1.12 s and 1.47 s is due to the propeller emergence shown in Fig. 26d. Strong correlation between the pitch motion and the wake field dynamics is seen. The wake fraction is at its minimum (meaning that the

inflow velocity into the propeller disk is close to free stream velocity) when the pitch motion is close to zero and the hull stern is just about to move downwards into the water. On the other hand, the wake fraction is at its maximum when the pitch motion is zero but the hull stern moving upwards out of water. The non-dimensional axial velocity contour in the shaft direction as well as the transverse velocity vectors for the simulation in calm water is shown in Fig. 27. Moreover, the non-dimensional axial velocity contours and the transverse velocity vectors for three time instances of the lowest, the mean level and the highest surface averaged wake fraction for simulations in waves are shown in Fig. 28 and Fig. 29. The bilge vortex found by the same Q-criterion are shown in Fig. 31. The bilge vortices in waves show interesting dynamics in comparison to calm water. They become stronger by increasing wave length. The position where the bilge vortices hit the propeller disk in calm water is more and less stationary, while they considerably move up and down in the disk when the waves are present. The other interesting phenomenon in waves is the existence of the secondary vortex system which is caused by the propeller shaft and enters the propeller disk.

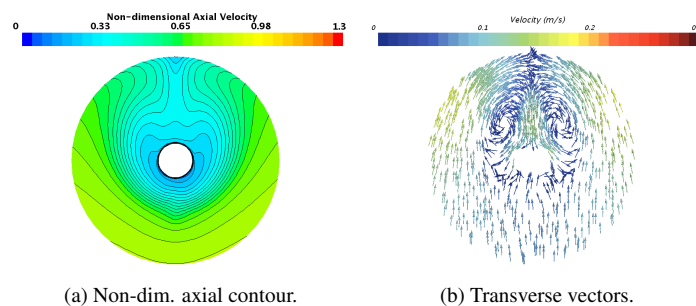


Figure 27: Velocity components on the propeller disk in calm water (Case 1).

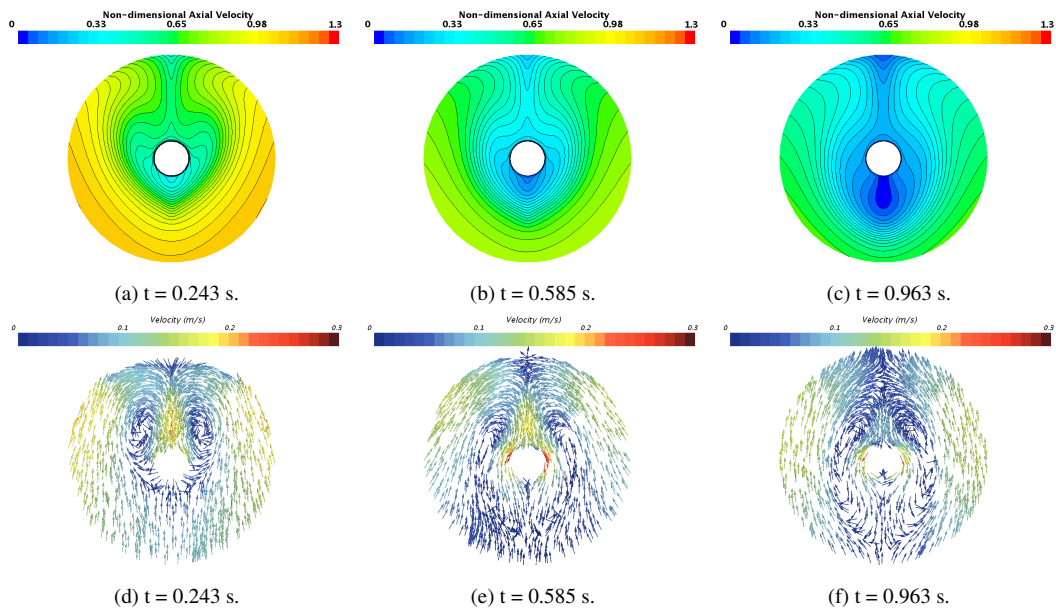


Figure 28: Non-dimensional axial velocity contours and transverse velocity vectors for Case 2 at three time instances; wake trough (a & d), mean wake (b & e) and wake peak (c & f).

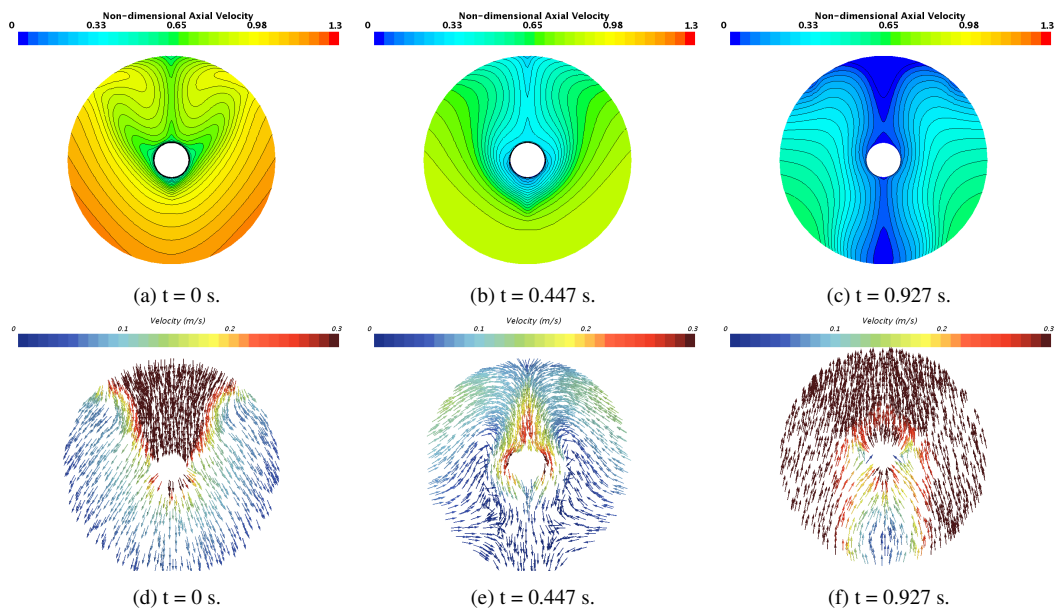


Figure 29: Non-dimensional axial velocity contours and transverse velocity vectors for Case 3 at three time instances; wake trough (a & d), mean wake (b & e) and wake peak (c & f).

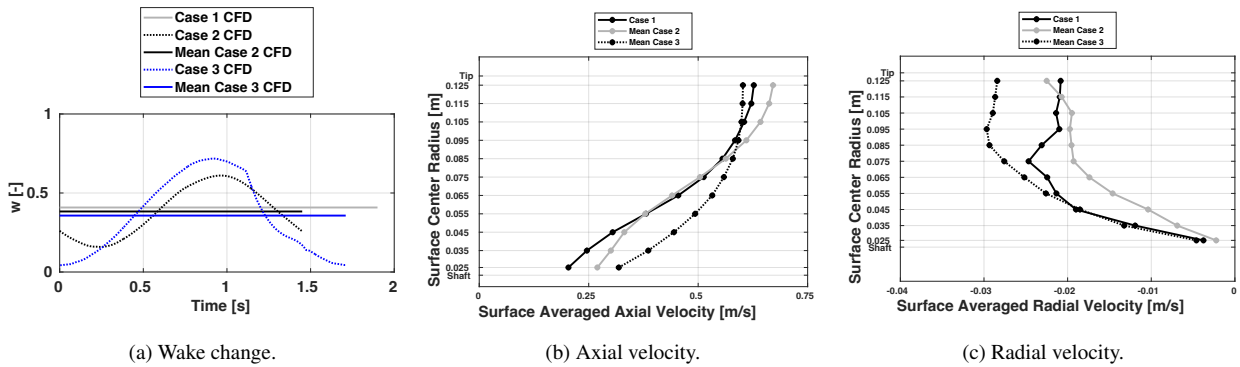


Figure 30: Variation of wake (a) and the mean surface averaged velocity components (b) and (c).

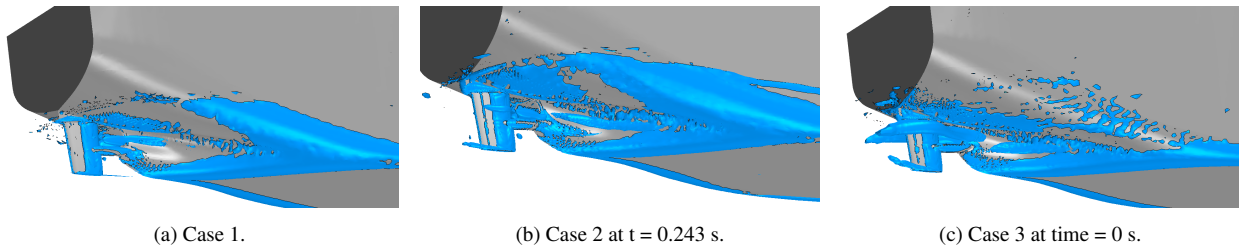


Figure 31: The bilge vortex found by Q-criterion = 7.5.

4.5 Conclusion

This is an ongoing research and so far we have managed to set up a robust method for capturing the dynamics of a ship wake field. The future plan is to investigate the correlation between the ship motions and the wake dynamics more in detail. As a complementary approach to what we have carried out so far, we plan to study the isolated effects from the waves as well as the ship motions on the flow into propeller.

5 Towards Uncertainty Analysis of CFD Simulation of Ship Responses in Regular Head Waves

Ship hydrodynamic performance prediction in waves is a common practice in the early stages of the ship design process as the interaction between the ship and waves may adversely affect the hydrodynamic responses of the ship in comparison to calm water. Various well-established numerical and experimental methods are often utilized for prediction of ship performance in waves. Although the model tests are expensive and time-consuming, a high level of accuracy is often achieved in such experiments. On the other hand, with respect to the increased computational power, prediction of ship performance in waves by the numerical methods based on Computational Fluid Dynamics (CFD) techniques are gradually acquiring more popularity. However, the validity of the incorporated discretization schemes and modelling assumptions in these state-of-the-art CFD methods are often overlooked and the method accuracy is mainly assessed through the validation of the results based on the respective model test data. Validation as an engineering exercise aims to show that the right equations are solved, while verification (mathematical exercise) is required to demonstrate that equations are solved right Roache (1998).

The eventual objective of this research is to perform verification and validation exercises of a ship performance prediction in regular head waves using CFD, whereas in this part of the work, the working progress is presented which may be subjected to significant revisions. To this end, extensive attempts have been made to investigate numerical wave propagation without the presence of the hull. Ship responses in waves are significantly influenced by the wave excitation forces. Therefore, not only high level of accuracy is required for the simulation of the numerical waves, but also quantification of the numerical uncertainties are of a great importance. This becomes even more challenging when the ship hydrodynamic responses, such as motions and added resistance in waves, exhibit dependencies on wave steepness. In this part of the work, the main focus of such uncertainty analyses is on the systematic grid convergence study.

5.1 Method description

The second variant of the MOERI tanker (KVLCC2) in model-scale (scale factor = 100) and operating in fresh water at the design speed (Froude number $Fr = 0.142$) in a regular head wave (wave height $H = 0.06$ m and wave length $\lambda/L = 0.6$) is considered. The model tests are carried out in Osaka University Towing Tank.

In this part of the work, a commercial CFD solver, Simcenter STAR-CCM+ (version 2020.3.1), is used with

an Unsteady Reynolds-Averaged Navier-Stokes (URANS) approach. Unstructured grids including the trimmed hexahedral meshes with local refinements near the free surface and near the hull as well as prism layer meshes along the hull surface are generated using STAR-CCM+ automatic mesh generator. Different cautions are taken into account to eliminate/diminish undesired diffusion depths (transition zone between two local refinement zones) and also to generate "as geometrically similar as possible" set of unstructured grids. The computational domain in each grid is discretized employing an Overset Topology which consists a moving overset region and a stationary background region with specific treatment of cell sizes near the overlapping regions (where the information is exchanged between the background and overset regions).

The simulations are mainly carried out for five different grid sets shown in Table 9, in which the effects of different local refinement zones as well as the quality of the cell size and overset interpolations in the overlapping zones are evaluated. The simulations are carried out in three different computational domain widths, i.e., Quasi-2D (only one cell in Y direction), Small Width SW-3D (one third of the full domain in Y) and Full Width FW-3D (full domain size in Y). The reason behind choosing one third of the domain size for the SW-3D case is to eliminate undesired diffusion depths that may be introduced by the grid generator.

Table 9: Grid sets details.

Grid Set No.	Simulation Type	Regions		Local Refinement Zones					Prism Layers
		Background	Overset	Free Surface	Kelvin Wedge	Overlapping	Around Overset	Inside Overset	
1	Wave Propagation	✓	–	✓	–	–	–	–	–
2	Wave Propagation	✓	–	✓	✓	✓	✓	–	–
3	Wave Propagation	✓	✓ Restricted	✓	✓	✓	✓	✓	–
4	Wave Propagation	✓	✓ Predefined Motions	✓	✓	✓	✓	✓	–
5	Hull Performance	✓	✓ Hull Motions	✓	✓	✓	✓	✓	✓

In each grid set, four systematically refined grids are considered which are determined by the refinement levels $n = 1.0$ (coarsest), 1.5, 2.0 and 2.5 (finest). Trimmed hexahedral meshes (isotropic volume meshes) are generated in both the background and the overset regions, where every two cells are divided into $2n$ cells in each direction (except in Y for Quasi-2D simulations) to derive a geometrically similar grids. Figure 32 shows the grids ($n = 1$ and 1.5) in the grid set number 2 where different local refinement zones are illustrated by different colors.

In order to achieve geometrically similar anisotropic sub-layer (prism layer) meshes, the methodology presented by Crepier (2017) is employed. In this method, the total thickness of prism layers remains the same between the grids but both the first layer cell thickness and the growth ratio between the layers are adjusted accordingly. The total number of layers in each grid will be nN_t , in which N_t is the total number of layers for the coarsest grid, see Figure 33. The prism layers are generated such that the non-dimensional wall distance y^+ remains above 30 over the major part of the hull surface during the ship simulations in waves (for all grids in the grid set number 5), hence a wall function is utilized.

An overview of the computational domain size and the imposed boundary conditions are shown in Figure 34. Although the Quasi-2D simulations are computationally much cheaper than 3D simulations, it was found that the Quasi-2D results for the wave propagation simulations are not necessarily similar to that of 3D cases. Therefore, the wave propagation simulations are mainly performed in SW-3D domain in order to gain similar results as of FW-3D while keeping the computational costs low. Thereafter, the hull performance simulations are carried out only in the FW-3D domain.

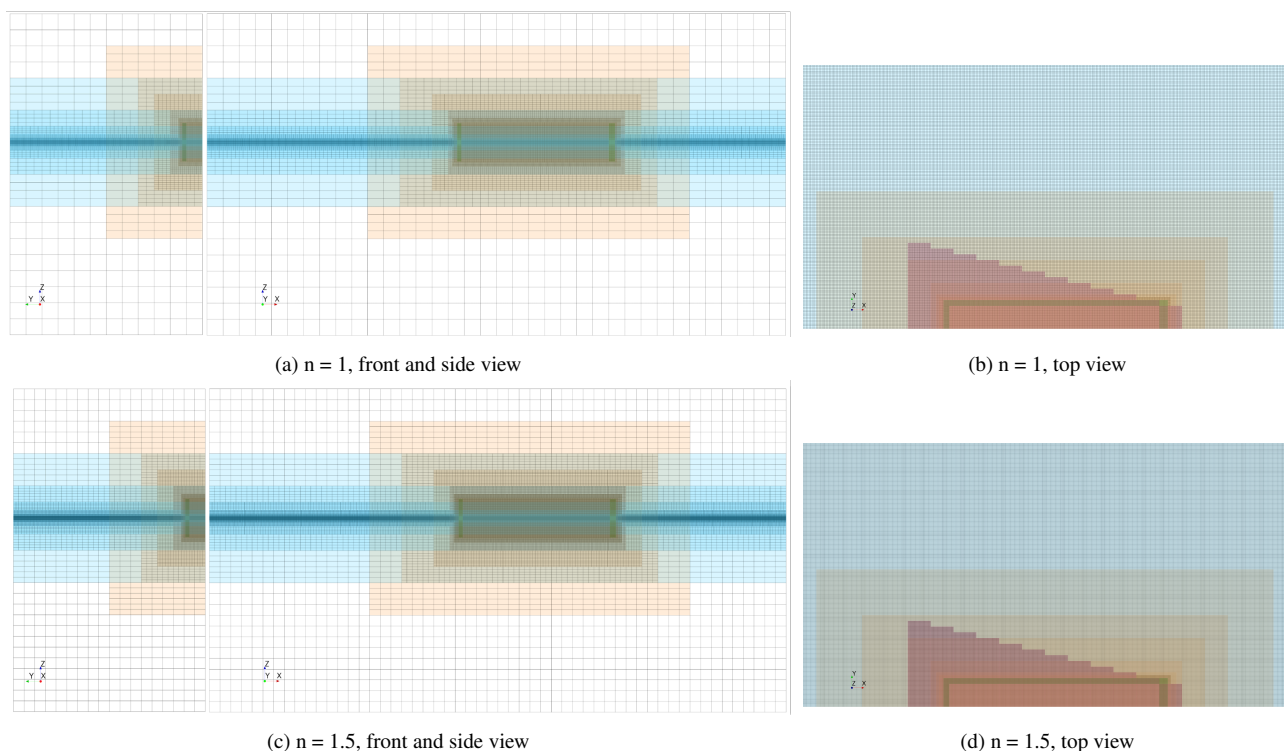


Figure 32: Overview of the grids and local refinement zones (Free Surface Around Overset Overlapping Kelvin Wedge) in the grid set number 2 (FW-3D).

The Volume of Fluid (VOF) model is used to capture the free surface. A wave forcing function is used in the

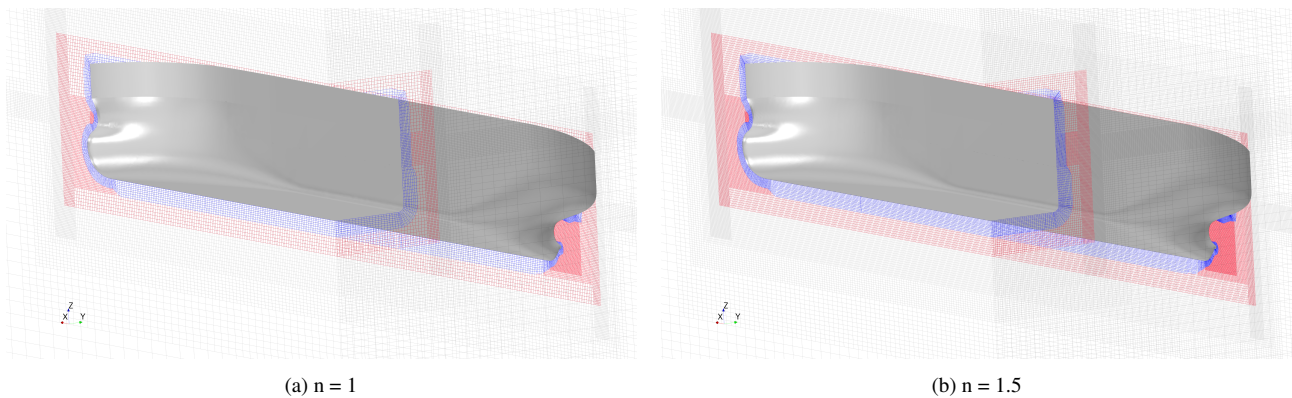


Figure 33: Overview of the grids near the hull in the grid set number 5. Black lines represents the mesh in the background region. Blue and red colors represent the isotropic and prism layer meshes in the overset region, respectively. Local refinement zones inside the overset can also be observed.

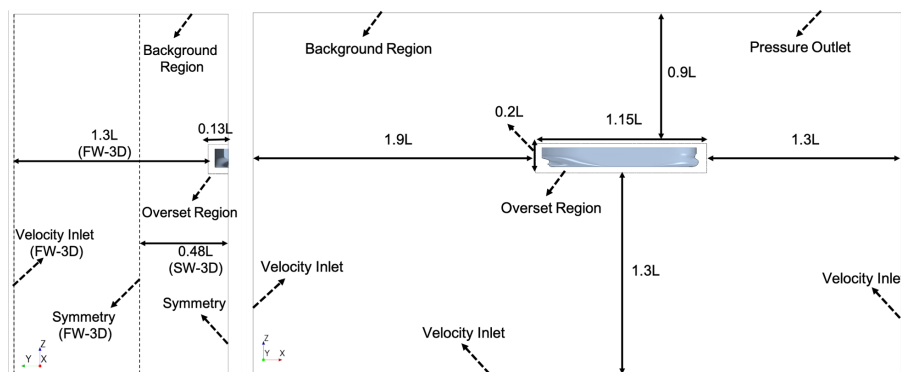


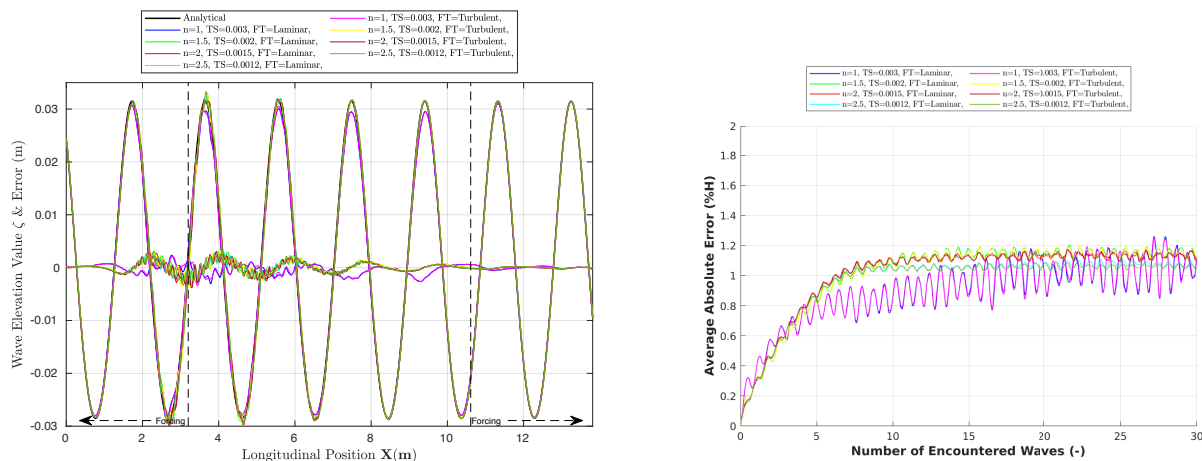
Figure 34: Computational domain size and boundary conditions.

vicinity of all vertical boundaries with velocity inlet boundary conditions. An implicit unsteady solver is used with a second order temporal discretizational scheme (time step $t = 0.003/n$, hence similar Courant number between the grids in each grid set).

5.2 Results and discussion

The numerical wave elevation ζ and its error (relative to the analytical wave) after 30 encountered waves are presented for the grid set 1 (SW-3D domain) in Figure 35a. Moreover, the longitudinally averaged absolute error (in percentage of the wave height) for Laminar and Turbulent flow ($k-\omega$ SST) simulations are presented in Figure 35b. The results of the turbulent flow simulations are similar to that of laminar flow. Wave propagation is a laminar phenomenon by its nature, while turbulent simulations are required when the hull performance is being studied.

The averaged absolute error is rather low for both laminar and turbulent flow simulations in the grid set number 1. Moreover, the error converges approximately after a few encountered wave periods. Therefore,



(a) Wave elevation after 30 encountered periods

(b) Monitored averaged absolute error

Figure 35: Wave elevation and its error with respect to the analytical wave for the grid set number 1 in SW-3D domain. TS = time step and FL = Flow Type.

the simulations deemed converged after 15 encountered waves and the Fourier analysis of the wave elevation at some probes are carried out for grid sets 1 and 2 over the 15-20 encountered waves time window, see Figure 36. The probes are located at specific distances from the inlet representing: end of forcing zone, before the overset region, within the overlapping zone and inside the overset region close to the hull fore perpendicular (notice that the hull was not present in these simulations and it is just illustrated for clarification of probe locations.)

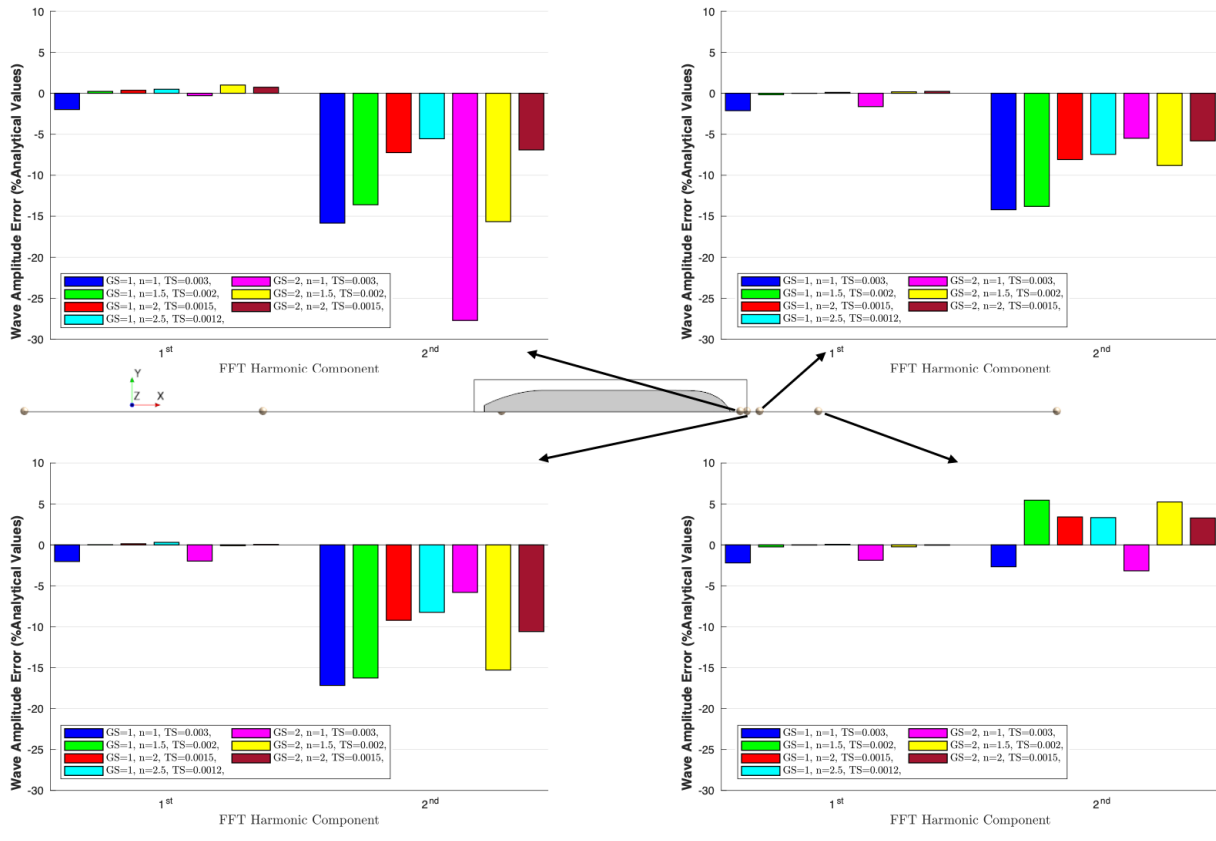


Figure 36: The Fourier analysis results of the wave elevation at specific probes for the grid sets 1 and 2 (SW-3D) for turbulent flow simulations. The hull illustration is only for clarification of probe locations and it was not present in these simulations.

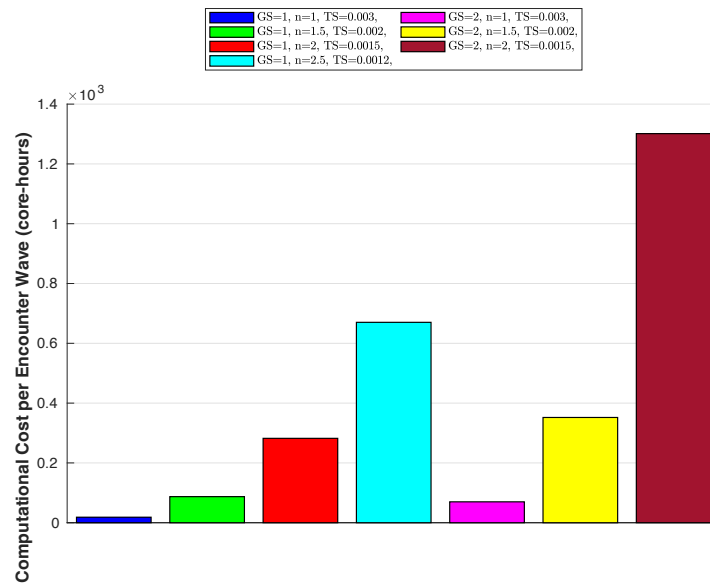


Figure 37: The computational costs for grid sets 1 and 2 for turbulent flow simulations. GS = Grid Set.

In Figure 36 the first and second harmonic amplitudes of the wave elevation are compared with the analytical values. The first harmonic amplitude is quite low for all grids in both grid sets, except for the coarsest grid ($n = 1$). Relatively larger errors are seen for the second harmonic amplitude, however, the second harmonic amplitude value is significantly smaller than the first harmonic component, hence it incorporates larger error when it is compared to the analytical value. One interesting point is that the second harmonic amplitude error is reduced from the coarsest grid to the finest one in the grid set number 1, while it does not show the same trend in the grid set number 2. More studies are in progress on such matter. The computational costs per each encountered wave period in terms of core-hours are provided in Figure 37. The computational costs are clearly much higher for the finer grids in each grid set.

Detailed Fourier analysis is planned to be carried out for different probes in different time windows and more results are going to be provided related to the grid set 3-5. Moreover, the uncertainty analyses of the results are going to be carried out for the harmonic amplitudes.

6 Concluding remarks and future work

Conclusions and discussion related to different part of this research project have been separately provided in the end of each part. In summary, the results from this project showed the importance of Verification and Validation (V&V) of ship motion and added resistance predictions in waves. Since the process of V&V for computational prediction of ship performance in waves is a very time-consuming task, most of the research carried out in this field opt not to investigate the uncertainty of the predicted results (often only V&V is done in calm water which is more straight forward but not extendable to the results obtained from simulations in waves). In the first part of 'Propeller-Hull Interaction Effects in Waves' project we highlight the importance of V&V and started to obtain the uncertainty of the wave propagation, ship motions and added resistance results in waves. Now we have gained more confidence in our computational setup and know the uncertainty of the predictions using different methods more in detail. The uncertainty analysis of the open water and self-propulsion simulations in waves will be carried out in 2022, in the second part of the project. Knowing the uncertainty of the computed motions, added resistance and added power in waves are inevitable for accurately predicting a ship's performance in waves. After finalizing the uncertainly, we continue to work on an isolated (open water) propeller performance degradation in waves based on a series of test which we have carried out at SSPA's towing tank. Next step will be running self-propulsion simulation in waves and calm water to map the propeller-hull interaction effect.

References

- V. Bertram. *Practical Ship Hydrodynamics*. Butterworth-Heinemann, Oxford, second edition, 2012.
- V. Bertram. Added power in waves - time to stop lying (to ourselves). In *Proceedings of the 1st Hull Performance & Insight Conference (HuLLPIC)*, pages 5–13, Pavone, 2016.
- J. J. Block. *The resistance increase of a ship in waves*. PhD thesis, Delft University of Technology, 1993.
- P. Boese. Eine einfache methode zur berechnung der widerstandserhöhung eines schiffes im seegang. Technical report, institut für schiffbau der universität hamburg., 1970. (in German).
- F. Coslovich, M. Kjellberg, M. Östberg, and C.-E. Janson. Added resistance, heave and pitch for the KVLCC2 tanker using a fully nonlinear unsteady potential flow boundary element method. *Ocean Engineering*, 229: 108935, 2021. ISSN 0029-8018. doi: 10.1016/j.oceaneng.2021.108935.
- P. Crepier. Ship resistance prediction: verification and validation exercise on unstructured grids. In *Proceedings of the 7th International Conference on Computational Methods in Marine Engineering (MARINE)*, pages 365–376, Nantes, France, 2017. ISBN 978-84-946909-8-3.
- G. Ducrozet, H. B. Bingham, A. P. Engsig-Karup, and P. Ferrant. High-order finite difference solution for 3D nonlinear wave-structure interaction. *Journal of Hydrodynamics*, 22(5):225–230, 2010. doi: 10.1016/S1001-6058(09)60198-0.
- A. P. Engsig-Karup, H. B. Bingham, and O. Lindberg. An efficient flexible-order model for 3D nonlinear water waves. *Journal of Computational Physics*, 228(6):2100–2118, 2009. ISSN 0021-9991. doi: 10.1016/j.jcp.2008.11.028.
- O. M. Faltinsen. *Sea loads on ships and offshore structures*. Cambridge Ocean Technology Series. Cambridge University Press, Cambridge, UK, 1990. ISBN 9780521458702.
- O. M. Faltinsen, K. J. Minsaas, N. Liapis, and S. O. Skjørdal. Prediction of resistance and propulsion of a ship in a seaway. In *Proceedings of the 13th Symposium on Naval Hydrodynamics*, pages 505–529, Tokyo, 1980.
- J. Fenton. A fifth-order stokes theory for steady waves. *Journal of Waterway, Port, Coastal and Ocean Engineering*, 111(2):216–234, 1985. doi: 10.1061/(ASCE)0733-950X(1985)111:2(216).

- J. Gerritsma and W. Beukelman. Analysis of the resistance increase in waves of a fast cargo ship. *International Shipbuilding Progress.*, 19(217):285–293, 1972. ISSN 0020868X. doi: 10.3233/isp-1972-1921701.
- J. Gerritsma, J. van den Bosch, and W. Beukelman. Propulsion in regular and irregular waves. *International Shipbuilding Progress*, 8(82):235–247, 1961. doi: 10.3233/ISP-1961-88201.
- T. H. Havelock. The resistance of a ship among waves. *Proceedings of the Royal Society of London. Series A - Mathematical and Physical Sciences.*, 161(906):299–308, 1937. doi: 10.1098/rspa.1937.0147.
- T. H. Havelock. XLVII. The drifting force on a ship among waves. *The London, Edinburgh, and Dublin Philosophical Magazine and Journal of Science.*, 33(221):467–475, 1942. doi: 10.1080/14786444208521213.
- T. Hino, F. Stern, L. Larsson, M. Visonneau, N. Hirata, and J. Kim, editors. *Numerical Ship Hydrodynamics - An Assessment of the Tokyo 2015 Workshop*. Springer, 2021. doi: 10.1007/978-3-030-47572-7.
- S. E. Hirdaris, Y. Lee, G. Mortola, A. Incecik, O. Turan, S. Y. Hong, B. W. Kim, K. H. Kim, S. Bennett, S. H. Miao, and P. Temarel. The influence of nonlinearities on the symmetric hydrodynamic response of a 10,000 teu container ship. *Ocean Engineering*, 111:166–178, 2016. ISSN 0029-8018. doi: 10.1016/j.oceaneng.2015.10.049.
- M. Irannezhad, A. Eslamdoost, and R. E. Bensow. Numerical investigation of a large diameter propeller emergence risk for a vessel in waves. In *Proceedings of the 8th International Conference on Computational Methods in Marine Engineering (MARINE)*, pages 634–645, Gothenburg, Sweden, 2019. doi: 10.5281/zenodo.2650219.
- M. Irvine, J. Longo, and F. Stern. Pitch and heave tests and uncertainty assessment for a surface combatant in regular head waves. *Journal of Ship Research*, 2008. ISSN 00224502.
- ITTC, 2011. International Towing Tank Conference. Recommended Procedures and Guidelines, VPractical Guidelines for Ship CFD Applications., 26th ITTC.
- ITTC, 2017. International Towing Tank Conference. Recommended Procedures and Guidelines 7.5-02-07-02.5, “Verification and Validation of Linear and Weakly Nonlinear Seakeeping Computr Codes”, 28th ITTC, 2017.

- ITTC, 2018. International Towing Tank Conference. Recommended Procedures and Guidelines 7.5-02-07-02.8, “Calculation of the weather factor f_w for decrease of ship speed in wind and waves”, 29th ITTC, 2018.
- S. A. G. Joncquez, H. B. Bingham, P. Andersen, and D. Kring. Validation of added resistance computations by a potential-flow boundary-element method. In *Proceedings of the 27th Symposium on Naval Hydrodynamics*. Office of Naval Research, U.S.A., 2008.
- W. P. A. Joosen. Added resistance of ships in waves. In *Proceedings of the 6th Symposium on Naval Hydrodynamics*., pages 637–647, National Academy Press., Washington D.C.,USA, 1966.
- M. Kjellberg. *Fully non-linear unsteady three-dimensional boundary element method for ship motions in waves*. PhD thesis, Chalmers University of Technology, 2013.
- L. Larsson and H. C. Raven. *Ship Resistance and Flow*. PNA Series. Society of Naval Architects and Marine Engineers, Jersey City, 2010.
- L. Larsson, F. Stern, and M. Visonneau, editors. *Numerical Ship Hydrodynamics - An Assessment of the Gothenburg 2010 Workshop*. Springer, 2014. doi: 10.1007/978-94-007-7189-5.
- C.-M. Lee, J.-H. Seo, J.-W. Yu, J.-E. Choi, and I. Lee. Comparative study of prediction methods of power increase and propulsive performances in regular head short waves of KVLCC2 using CFD. *International Journal of Naval Architecture and Ocean Engineering*, 11(2):883–898, 2019. ISSN 2092-6782. doi: 10.1016/j.ijnaoe.2019.02.001.
- J. Lee, D.-M. Park, and Y. Kim. Experimental investigation on the added resistance of modified KVLCC2 hull forms with different bow shapes. *Proceedings of the Institution of Mechanical Engineers, Part M: Journal of Engineering for the Maritime Environment*, 231(2):395–410, 2017. doi: 10.1177/1475090216643981.
- E. V. Lewis. Principles of naval architecture. 2nd reversion, vol III Motions in waves and controllability, 1989. ISSN 0023-6837.
- P. M. Best practices for simulations with waves., 2017.
- M. A. Martinsen. A design tool for estimating the added wave resistance of container ships. Master’s thesis, Technical University of Denmark, 2016.
- H. Maruo. The excess resistance of a ship in rough seas. *International Shipbuilding Progress*., 4, no. 35: 337–345, 1957. doi: 10.3233/ISP-1957-43501.

- H. Maruo. The drift of a body floating on waves. *Journal of Ship Research.*, 4:1–10, 1960.
- A. Mola, L. Heltai, and A. De Simone. Wet and dry transom stern treatment for unsteady and nonlinear potential flow model for naval hydrodynamics simulations. *Journal of Ship Research*, 61(1):1–14, 2017. doi: 10.5957/JOSR.61.1.160016.
- D. I. Moor and D. C. Murdey. Motions and propulsion of single screw models in head seas, Part II. *Transactions of the Royal Institution of Naval Architects*, 112(2), 1970.
- S. Muzafferija and M. Perić. *Computation of free-surface flows using interface-tracking and interface-capturing methods.*, pages 59–100. WIT Press, Computational Mechanics Publications, 01 1999.
- S. Nakamura and S. Naito. Propulsive performance of a container ship in waves. *Journal of the Society of Naval Architects of Japan*, 15(158):24–48, 1975.
- J. N. Newman. The drift force and moment on ships in waves. *Journal of Ship Research.*, 11:51–60, 1967.
- P. J. Roache. Verification of codes and calculations. *AIAA Journal*, 36(5):696–702, 1998. doi: 10.2514/2.457.
- H. Sadat-Hosseini, P.-C. Wu, P. Carrica, H. Kim, Y. Toda, and F. Stern. CFD verification and validation of added resistance and motions of KVLCC2 with fixed and free surge in short and long head waves. *Ocean Engineering*, 59:240–273, 02 2013. doi: 10.1016/j.oceaneng.2012.12.016.
- N. Salvesen. Added resistance of ships in waves. *Journal of Hydronautics*, 12(1):24–34, 1978. doi: 10.2514/3.63110.
- J.-H. Seo, C.-M. Lee, J.-W. Yu, J.-E. Choi, and I. Lee. Power increase and propulsive characteristics in regular head waves of KVLCC2 using model tests. *Ocean Engineering*, 216:108058, 2020. ISSN 0029-8018. doi: 10.1016/j.oceaneng.2020.108058.
- C. D. Simonsen, J. F. Otzen, S. Joncquez, and F. Stern. EFD and CFD for KCS heaving and pitching in regular head waves. *Journal of Marine Science and Technology (Japan)*, 2013. ISSN 09484280. doi: 10.1007/s00773-013-0219-0.
- B. Taskar, S. Steen, R. E. Bensow, and B. Schröder. Effect of waves on cavitation and pressure pulses. *Applied Ocean Research*, 60:61–74, 2016a. ISSN 0141-1187. doi: doi.org/10.1016/j.apor.2016.08.009.

- B. Taskar, K. K. Yum, S. Steen, and E. Pedersen. The effect of waves on engine-propeller dynamics and propulsion performance of ships. *Ocean Engineering*, 122:262–277, 2016b. doi: 10.1016/j.oceaneng.2016.06.034.
- P. Valanto and Y. Hong. Wave added resistance and propulsive performance of a cruise ship in waves. In *Proceedings of the 27th International Ocean and Polar Engineering Conference*, pages 737–745, San Francisco, CA, USA, 2017. International Society of Offshore and Polar Engineers (ISOPE).
- P.-C. Wu. *A CFD Study on Added Resistance, Motions and Phase Averaged Wake Fields of Full Form Ship Model in Head Waves*. PhD thesis, Osaka University, 2013.
- J.-W. Yu, C.-M. Lee, J.-E. Choi, and I. Lee. Effect of ship motions on added resistance in regular head waves of KVLCC2. *Ocean Engineering*, 146:375 – 387, 2017. ISSN 0029-8018. doi: 10.1016/j.oceaneng.2017.09.019.

Lighthouse brings together industry, society, academia and institutes in triple helix collaboration to strengthen Sweden's maritime competitiveness through research, development and innovation. As part of the work for a sustainable maritime sector, Lighthouse initiates and coordinates relevant research and innovation based on industry and society's needs.

Lighthouse – for a competitive, sustainable and safe maritime sector with a good working environment



LIGHTHOUSE PARTNERS



LIGHTHOUSE ASSOCIATE MEMBERS

